The Astronomical Journal, 165:83 (20pp), 2023 March https://doi.org/10.3847/1538-3881/acab6b

Mass Production of 2021 KMTNet Microlensing Planets II

Yoon-Hyun Ryu[1], In-Gu Shin[2], Hongjing Yang[3], Andrew Gould[4,5], Michael D. Albrow[6], Sun-Ju Chung[1,7], Cheongho Han[8], Kyu-Ha Hwang[1], Youn Kil Jung[1], Yossi Shvartzvald[9], Jennifer C. Yee[2], Weicheng Zang[3], Sang-Mok Cha[1,10], Dong-Jin Kim[1], Seung-Lee Kim[1,7], Chung-Uk Lee[1,7], Dong-Joo Lee[1], Yongseok Lee[1,10], Byeong-Gon Park[1,7], and Richard W. Pogge[5]

[1] Korea Astronomy and Space Science Institute, Daejon 34055, Republic of Korea; yhryu@kasi.re.kr
[2] Center for Astrophysics | Harvard & Smithsonian, 60 Garden St., Cambridge, MA 02138, USA
[3] Department of Astronomy and Tsinghua Centre for Astrophysics, Tsinghua University, Beijing 100084, People's Republic of China
[4] Max-Planck-Institute for Astronomy, Königstuhl 17, D-69117 Heidelberg, Germany
[5] Department of Astronomy, Ohio State University, 140 W. 18th Ave., Columbus, OH 43210, USA
[6] University of Canterbury, Department of Physics and Astronomy, Private Bag 4800, Christchurch 8020, New Zealand
[7] Korea University of Science and Technology, Korea, (UST), 217 Gajeong-ro, Yuseong-gu, Daejeon, 34113, Republic of Korea
[8] Department of Physics, Chungbuk National University, Cheongju 28644, Republic of Korea
[9] Department of Particle Physics and Astrophysics, Weizmann Institute of Science, Rehovot 76100, Israel
[10] School of Space Research, Kyung Hee University, Yongin, Kyeonggi 17104, Republic of Korea
Received 2022 July 15; revised 2022 December 8; accepted 2022 December 11; published 2023 February 2

Abstract

We continue our program of publishing all planets (and possible planets) found by eye in 2021 Korea Microlensing Telescope Network (KMTNet) online data. We present four planets (KMT-2021-BLG-0712Lb, KMT-2021-BLG-0909Lb, KMT-2021-BLG-2478Lb, and KMT-2021-BLG-1105Lb), with planet-to-host mass ratios in the range $-3.3 \lesssim \log q \lesssim -2.2$. This brings the total of secure, by-eye, 2021 KMTNet planets to 16, including 8 in this series. The by-eye sample is an important check of the completeness of semiautomated detections, which are the basis for statistical analyses. One of the planets, KMT-2021-BLG-1105Lb, is blended with a relatively bright (I, V) $\sim$ (18.9, 21.6) star that may be the host. This could be verified immediately by high-resolution imaging. If so, the host is an early G dwarf, and the planet could be characterized by radial velocity observations on 30 m class telescopes.

Unified Astronomy Thesaurus concepts: Gravitational microlensing (672)

Supporting material: data behind figures

1. Introduction

In this paper, we continue the program outlined in Paper I (Ryu et al. 2022) to ensure the publication of all planets from the Korea Microlensing Telescope Network (KMTNet; Kim et al. 2016) 2021 season. As discussed there, many planets will be published as single-planet papers, either because of their intrinsic scientific interest or as an entry point of scientific work by junior workers. Many others will be published in small groups that are related by some common thread. However, robust statistical investigation requires that all planets be published, or at least be subjected to publication-quality analysis. The experience of the 2018 season, which is the first to be completed (Gould et al. 2022a; Hwang et al. 2022; Jung et al. 2022; Wang et al. 2022), shows that, even several years after the close of that season, six planets that had been detected by eye remained unpublished, while several dozen other "possible planets" required detailed investigation to determine that they were either nonplanetary or ambiguous in nature. There were, in addition, 11 planets discovered by the KMT AnomalyFinder system (Zang et al. 2021b, 2022) that had not previously been found by eye. As many dozens of KMTNet planets remain to be published from the 2016, 2017, and 2019 seasons, it seems prudent not to fall behind in the publication of 2021 planets.

As also noted in Paper I, the investigation and publication of all by-eye discoveries serves as an important check on the AnomalyFinder system. For 2018, two by-eye discoveries were not recovered by AnomalyFinder: OGLE-2018-BLG-0677 (Herrera-Martin et al. 2020), which failed to meet the selection criteria, and KMT-2018-BLG-1996 (Han et al. 2021b), which was recovered in the machine phase of AnomalyFinder but was not finally selected by eye. Among the $\sim$70 previously discovered planets from 2016–2019 that met the selection criteria, KMT-2018-BLG-1996 was one of only two that were not recovered. This was an important check on the completeness of AnomalyFinder. It is important to maintain this check as the years go forward, and for this reason, the analysis and publication of 2021 events prior to the application of AnomalyFinder are crucial to maintaining the robustness of this check.

In Paper I, we began this process by systematically going through the planetary candidates that had been selected by Y.-H.R., rank ordered by the preliminary estimates of planet-to-host mass ratio, q. We published four planets (KMT-2021-BLG-1391, KMT-2021-BLG-1253, KMT-2021-BLG-1372, and KMT-2021-BLG-0748), with finally adopted mass ratios $-4.4 \lesssim \log q \lesssim -2.9$.

In the present paper, we continue this approach. We analyze four planetary events (KMT-2021-BLG-0712, KMT-2021-BLG-0909, KMT-2021-BLG-2478, and KMT-2021-BLG-1105).

From the standpoint of future statistical studies it is just as important to decisively reject initially plausible candidates from

Table 1
Event Names, Cadences, Alerts, and Locations

Name	Γ (hr^{-1})	Alert Date	R.A.$_{J2000}$	Decl.$_{J2000}$	l	b
KMT-2021-BLG-0712	4.0	2021 May 1	17:57:08.56	−31:11:04.09	−0.66	−3.29
KMT-2021-BLG-0909	1.0	2021 May 19	17:42:28.85	−27:38:20.90	+0.75	+1.27
KMT-2021-BLG-2478	4.0	2021 Sep 14	17:57:14.21	−29:06:07.09	+1.16	−2.27
KMT-2021-BLG-1105	1.0	2021 Jun 2	17:42:55.74	−25:30:32.08	+2.61	+2.30

Note. The coordinates given here are for the nearest catalog stars (i.e., baseline objects). In Section 4 we discuss the offsets from these locations of the actual events.

the final sample as it is to populate the sample. This statement is most directly applicable to candidates that are objectively selected by AnomalyFinder. However, as there is strong overlap between by-eye and AnomalyFinder planets, the rejection of by-eye candidates can contribute substantially to this task. In Paper I, we reported that we rejected three such candidates (KMT-2021-BLG-0637, KMT-2021-BLG-0750, and KMT-2021-BLG-0278). We note that in the course of identifying the four planetary events analyzed here, we rejected four others: KMT-2021-BLG-0631 was eliminated because re-reduction showed that the apparent anomaly had been due to data artifacts, and KMT-2021-BLG-0296 and KMT-2021-BLG-1484 were both eliminated because they had low $\Delta\chi^2 < 30$ improvement relative to a point lens and (related to this) many competing solutions. In addition, KMT-2021-BLG-1360 was eliminated because the anomaly detection, although formally very significant, $\Delta\chi^2 = 170$, rests on a single point. One reason for rejecting such "detections" is that unexpected systematics can always corrupt a single point. Nevertheless, out of intellectual curiosity, we still conducted a systematic investigation of this event and found that it had multiple 2L1S solutions that span two decades in q, as well as 1L2S solutions, all at comparable χ^2. We mention this mainly as a caution regarding automated planet sensitivity calculations that rely solely on χ^2 criteria to determine whether a given simulated planet is "detectable." In this case, $\Delta\chi^2$ is substantially above the threshold of the KMT AnomalyFinder search algorithm (Zang et al. 2022), yet the "planet" (if that is what caused the anomaly) cannot be recovered even at order-of-magnitude precision.

Finally, we remark on the progress of publication of other 2021 KMTNet planets, which, as mentioned above, can be of individual or group interest. In the former category are KMT-2021-BLG-0912 (Han et al. 2022a), KMT-2021-BLG-1077 (two planets; Han et al. 2022d), KMT-2021-BLG-1898 (Han et al. 2022e), and KMT-2021-BLG-0240 (Han et al. 2022c), with the last of these probably being unusable for mass ratio studies because of a severe degeneracy in q. In the latter category are the three planetary events KMT-2021-BLG-0320, KMT-2021-BLG-1303, and KMT-2021-BLG-1554, which have the common characteristic of being sub-Jovian planets (Han et al. 2022b), and two others, KMT-2021-BLG-0171, and KMT-2021-BLG-1689 (Yang et al. 2022), which have the common characteristic of being discovered in a survey-plus-follow-up campaign. Note that while KMT-2021-BLG-0171 would have been discovered even without follow-up data, there are no KMT data during the anomaly in KMT-2021-BLG-1689. Hence, only the first of these two will enter the AnomalyFinder statistical sample. In addition, KMT-2021-BLG-0322 has been thoroughly investigated and found to be ambiguous as a binary-star system that may or may not contain a planet (Han et al. 2021a).

Thus, with the publication of this paper, there are a total of about 16 planets from 2021 that are suitable for mass ratio studies, which constitutes good initial progress.

2. Observations

All of the planets in this paper were identified in by-eye searches of KMT events that were announced by the KMT AlertFinder (Kim et al. 2018b) as the 2021 season progressed. As described in Paper I, KMTNet observes from three 1.6 m telescopes that are equipped with ($2° \times 2°$) cameras at CTIO in Chile (KMTC), SAAO in South Africa (KMTS), and SSO in Australia (KMTA), mainly in the I band, with 60 s exposures, but with 9% of the observations in the V band. The data were reduced using pySIS (Albrow et al. 2009), a form of difference image analysis (DIA; Tomaney & Crotts 1996; Alard & Lupton 1998). For publication, the light curves were re-reduced using the tender-loving care (TLC) version of pySIS. For each event, we manually examined the images during the anomaly to rule out image artifacts as a potential explanation for the light-curve deviations.

None of the events reported here were alerted by any other survey, and, as far as we are aware, there were no follow-up observations.

As in Paper I, Table 1 gives the event names, observational cadences Γ, discovery dates, and sky locations.

3. Light-curve Analysis

3.1. Preamble

Our approach to analyzing events is identical to that described in Section 3.1 of Paper I. Here, we present only the definitions of the parameter symbols, in conformity with standard practice. For more details, we refer the reader to Paper I.

All of the events in this paper can be analyzed to a first approximation as 1L1S events, which are characterized by three Paczyński (1986) parameters (t_0, u_0, t_E), i.e., the time of lens−source closest approach, the impact parameter (normalized to the Einstein radius, θ_E), and the Einstein radius crossing time

$$t_E = \frac{\theta_E}{\mu_{rel}}; \quad \theta_E = \sqrt{\kappa M \pi_{rel}}, \quad \kappa \equiv \frac{4G}{c^2\,\mathrm{au}} \simeq 8.14\frac{\mathrm{mas}}{M_\odot}. \quad (1)$$

Here M is the mass of the lens, (π_{rel}, $\boldsymbol{\mu}_{rel}$) are the lens−source relative parallax and proper motion, $\mu_{rel} \equiv |\boldsymbol{\mu}_{rel}|$, and nLmS means "n lenses and m sources."

A 2L1S model always requires at least three additional parameters (s, q, α), i.e., the separation (normalized to θ_E) and mass ratio of the two lens components, as well as the angle between the line connecting these and the direction of $\boldsymbol{\mu}_{rel}$. If there are finite-source effects due to the source approaching or

crossing caustic structures that are generated by the lens, then one must also specify $\rho \equiv \theta_{\rm ast}/\theta_{\rm E}$, where $\theta_{\rm ast}$ is the angular radius of the source.

For 1L2S models, which can generate featureless bumps that can be mistaken for 2L1S "planets" (Gaudi 1998), the minimal number of parameters is 6, including $(t_{0,1}, t_{0,2})$ and $(u_{0,1}, u_{0,2})$ for the two times of closest approach and impact parameters, respectively, $t_{\rm E}$ for the Einstein timescale, and q_F, i.e., the flux ratio of the two sources in the I band. In many cases, one or both of the two normalized source radii must be specified, $\rho_1 = \theta_{\rm ast,1}/\theta_{\rm E}$ and $\rho_2 = \theta_{\rm ast,2}/\theta_{\rm E}$. More complex models involving orbital motion of the binary–source system may also be needed.

If the microlens parallax effect can be detected (or constrained), then one should include the microlens parallax vector (Gould 1992, 2000, 2004),

$$\boldsymbol{\pi}_{\rm E} = \frac{\pi_{\rm rel}}{\theta_{\rm E}} \frac{\boldsymbol{\mu}_{\rm rel}}{\mu_{\rm rel}}, \tag{2}$$

which is normally expressed in equatorial coordinates $\boldsymbol{\pi}_{\rm E} = (\pi_{{\rm E},N}, \pi_{{\rm E},E})$. In these cases, one usually must also fit, at least initially, for the first derivatives in time of the lens angular position, $\boldsymbol{\gamma} = [(ds/dt)/s,\ d\alpha/dt]$, because $\boldsymbol{\pi}_{\rm E}$ and $\boldsymbol{\gamma}$ can be correlated or even degenerate. In these cases, we restrict such fits to $\beta < 0.8$, where (An et al. 2002; Dong et al. 2009)

$$\beta \equiv \frac{\kappa M_\odot {\rm yr}^2}{8\pi^2} \frac{\pi_{\rm E}}{\theta_{\rm E}} \gamma^2 \left(\frac{s}{\pi_{\rm E} + \pi_{\rm s}/\theta_{\rm E}} \right)^3, \tag{3}$$

and where π_S is the source parallax.

In our initial heuristic analyses, we often predict $s_\pm^\dagger$ and α from the morphology of the light curve (Hwang et al. 2022; Ryu et al. 2022),

$$s_\pm^\dagger = \frac{\sqrt{4 + u_{\rm anom}} \pm u_{\rm anom}}{2}; \quad \tan\alpha = \frac{u_0}{\tau_{\rm anom}}, \tag{4}$$

under the assumption that the anomaly occurs when the source crosses the binary axis. Here $u_{\rm anom} = \sqrt{\tau_{\rm anom}^2 + u_0^2}$, $\tau_{\rm anom} = (t_{\rm anom} - t_0)/t_{\rm E}$, $t_{\rm anom}$ is the midpoint of the anomaly, and the "$\pm$" refers to major/minor-image perturbations. If there are two solutions, with normalized separation values $s_\pm$, as often occurs (see Zhang & Gaudi 2022 for a theoretical discussion of such degeneracies), we expect that the empirical quantity $s^\dagger = \sqrt{s_+ s_-}$ (without subscript) will be approximately equal to the subscripted quantity from Equation (4).

Finally, we often report the "source self-crossing time," $t_{\rm ast} \equiv \rho t_{\rm E}$. We note that this is a derived quantity and is not fit independently.

3.2. KMT-2021-BLG-0712

Figure 1 shows an otherwise standard 1L1S light curve with Paczyński (1986) parameters $(t_0,\ u_0,\ t_{\rm E}) = (9349.32,\ 0.145,\ 91\ {\rm days})$, punctuated by a 4.3-day double-horned profile, centered at $t_{\rm anom} = 9377.35$. The double-horned profile is unusual in that it has a smooth bump in the middle, which is almost certainly generated by the source approaching an interior wall of the caustic.

3.2.1. Heuristic Analysis

These parameters imply $\tau_{\rm anom} = 0.308$, $u_{\rm anom} = 0.340$, and thus

$$\alpha = 25°; \quad s_+^\dagger = 1.18. \tag{5}$$

Because the anomaly is clearly due to the source entering and leaving the caustic, we do not expect a degeneracy in s. Rather, we expect $s \simeq s_+^\dagger$.

3.2.2. Static Analysis

The grid search on the (s, q) plane returns only one solution, whose refinement with all parameters set free is shown in Table 2. We find that α and s are as expected, while $\log q = -3.3$ indicates a Saturn mass ratio planet. The caustic entrance and exit are both well covered, yielding a $\sim$8% measurement of a relatively low value of $\rho = 3.9 \times 10^{-4}$. We will see in Section 4.1 that this implies a large value of $\theta_{\rm E} \sim 0.64$ mas, and so a relatively nearby lens $\pi_{\rm rel} \sim 0.05\ {\rm mas}/(M/M_\odot)$ and thus a relatively large microlens parallax $\pi_{\rm E} \sim 0.08(\pi_{\rm rel}/0.05\ {\rm mas})$. Together with the relatively long timescale and the fact that the anomaly has three peaks (An & Gould 2001), this encourages us to search for microlens parallax solutions, in spite of the relatively faint source, $I_{S,{\rm KMTC01}} \sim 21.6$.

3.2.3. Parallax Analysis

As is almost always the case (except for some extremely long events), there are two parallax solutions, which are summarized in Table 2 and illustrated in Figure 2. As described in Section 3.1, we simultaneously fit for the first derivatives of the planet position due to its orbital motion $\boldsymbol{\gamma} = [(ds/dt)/s, d\alpha/dt]$. While Table 2 gives $\boldsymbol{\pi}_{\rm E}$ in standard equatorial coordinates, it is also useful to present these solutions in terms of the principal axes of the error ellipses,

$$(\pi_{{\rm E},\parallel},\ \pi_{{\rm E},\perp},\ \psi) = (+0.123 \pm 0.028,\ 0.40 \pm 0.11,\ 280.4°) \times [u_0 > 0] \tag{6}$$

and

$$(\pi_{{\rm E},\parallel},\ \pi_{{\rm E},\perp},\ \psi) = (+0.033 \pm 0.028,\ 0.72 \pm 0.14,\ 256.4°) \times [u_0 < 0]. \tag{7}$$

Here $\pi_{{\rm E},\parallel}$ (so called because, for short events, it is approximately parallel to the projected position of the Sun) is the minor axis of the error ellipse, $\pi_{{\rm E},\perp}$ is the major axis, and ψ is the angle of the minor axis, measured north through east. In line with the sign conventions of Figure 3 of Park et al. (2004; keeping in mind that MOA-2003-BLG-037 peaked after opposition while KMT-2021-BLG-0712 peaked before opposition), $\pi_{{\rm E},\parallel}$ is approximately west and $\pi_{{\rm E},\perp}$ is approximately north. Note that the actual projected orientation of Earth relative to the Sun at the peak is $\psi_\odot = 281.^\circ0$. Because the full width at half maximum of magnification versus time, $t_{\rm FWHM} \simeq \sqrt{12}\, u_0 t_{\rm E} \sim 45$ days, covers almost a radian of Earth's orbit, the "short event" approximation (Smith et al. 2003; Gould 2004; Park et al. 2004) is not expected to yield a precise characterization.

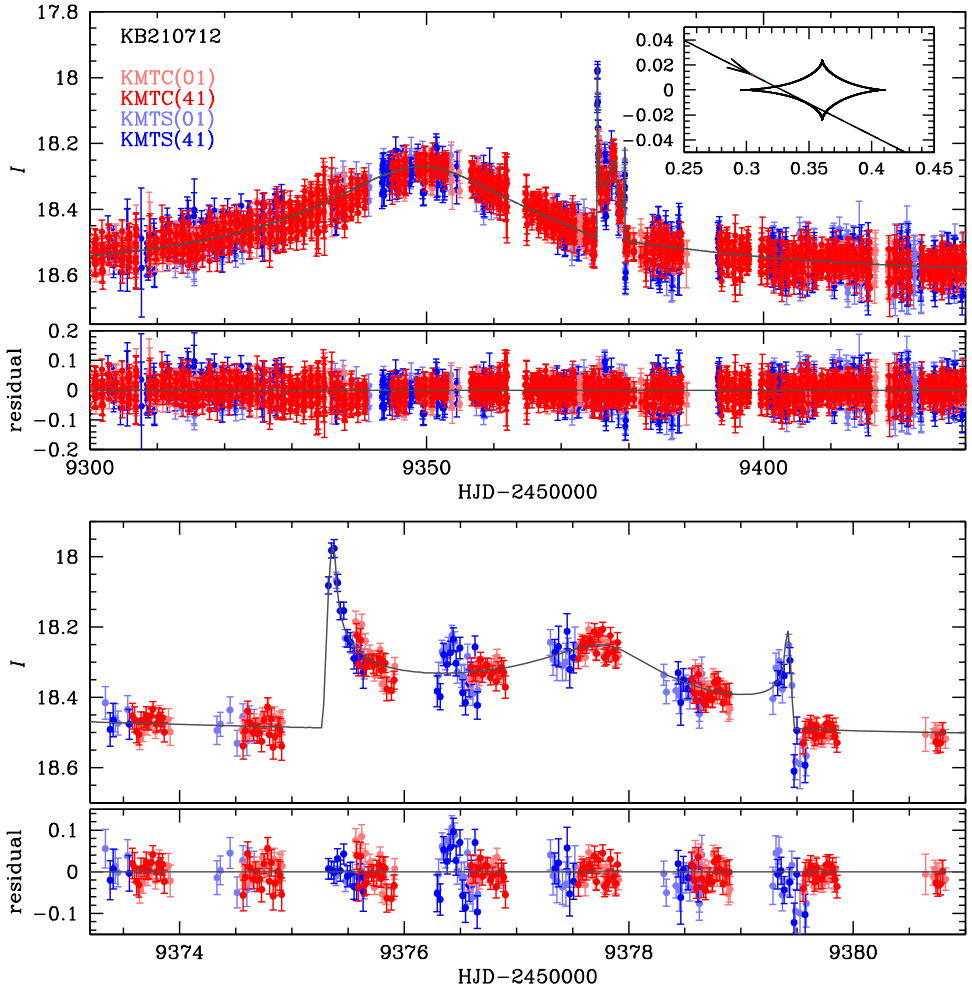

Figure 1. Light-curve data and models for KMT-2021-BLG-0712. Observations are color-coded by observatory and field, as indicated in the legend. Residuals to the model are shown for both the event as a whole (top) and the anomaly region (bottom). The source trajectory relative to the (major-image planetary) caustic is shown in the inset.

(The data used to create this figure are available.)

Table 2
Microlens Parameters for KMT-2021-BLG-0712

Parameters	Standard	Parallax Models	
		$u_0 > 0$	$u_0 < 0$
χ^2/dof	4263.666/4264	4224.244/4260	4222.276/4260
$t_0 - 2{,}459{,}340$	9.317 ± 0.115	9.954 ± 0.144	10.068 ± 0.129
u_0	0.147 ± 0.002	0.145 ± 0.002	-0.144 ± 0.002
t_E (days)	90.865 ± 0.951	88.503 ± 1.442	100.583 ± 2.039
s	1.196 ± 0.002	$1.196^{+0.016}_{-0.012}$	1.206 ± 0.020
q (10^{-4})	4.751 ± 0.141	$5.121^{+0.998}_{-0.654}$	5.653 ± 1.157
log q (mean)	-3.323 ± 0.014	-3.285 ± 0.062	-3.251 ± 0.079
α (rad)	0.467 ± 0.004	$0.452^{+0.027}_{-0.034}$	5.788 ± 0.039
ρ (10^{-4})	3.903 ± 0.330	4.010 ± 0.449	4.221 ± 0.551
$\pi_{E,N}$	...	0.425 ± 0.104	0.701 ± 0.111
$\pi_{E,E}$	...	-0.047 ± 0.034	-0.204 ± 0.042
ds/dt (yr^{-1})	...	$0.008^{+0.152}_{-0.199}$	-0.149 ± 0.262
$d\alpha/dt$ (yr^{-1})	...	$-0.688^{+0.415}_{-0.321}$	-0.902 ± 0.602
I_S [KMTC01,pySIS]	21.618 ± 0.013	21.644 ± 0.017	21.653 ± 0.018
I_B [KMTC01,pySIS]	18.676 ± 0.001	18.672 ± 0.002	18.673 ± 0.002
t_{ast} (hr)	0.851 ± 0.069	0.852 ± 0.092	1.019 ± 0.138

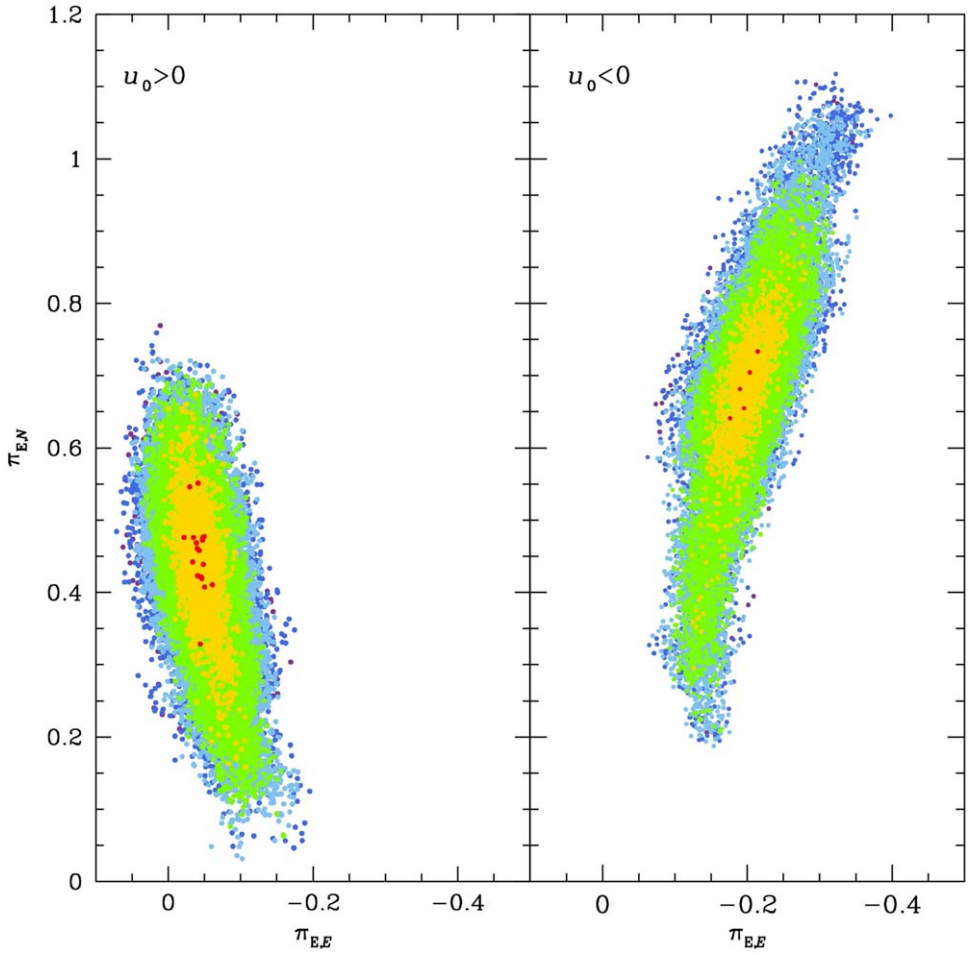

Figure 2. Scatter plot of MCMC trials in the $\boldsymbol{\pi}_{\rm E} = (\pi_{{\rm E},N}, \pi_{{\rm E},E})$ plane for the $u_0 > 0$ (left) and $u_0 < 0$ (right) solutions of KMT-2021-BLG-0712. Points are colored (red, yellow, green, cyan, blue) if they are $\Delta\chi^2 < (1, 4, 9, 16, 25)$ from the minimum.

We find, from fitting the event (with the anomaly removed) to a point-lens model with parallax, that the presence of the anomaly reduces the axes of the error ellipses for the two solutions from (0.030:0.45) to (0.028:0.11) and from (0.032:0.39) to (0.028:0.14), in particular, reducing the aspect ratios by factors of 3.8 and 2.4 for the two cases. This confirms the important role of the relatively complex caustic features in improving the parallax measurement.

3.3. KMT-2021-BLG-0909

Figure 3 shows an otherwise approximately standard 1L1S light curve with parameters $(t_0,\ u_0,\ t_{\rm E}) = (9354.1,\ 0.060,\ 16\ {\rm days})$, punctuated by a sharp bump, which erupts suddenly at 9360.65 and then peaks $\Delta t_{\rm rise} = 4$ hr later at $t_{\rm anom} = 9360.82$. This is almost certainly a caustic entrance, although there is no obvious caustic exit.

3.3.1. Heuristic Analysis

These parameters imply $\tau_{\rm anom} = 0.420$, $u_{\rm anom} = 0.424$, and thus

$$\alpha = 188^\circ.1; \quad s_+^\dagger = 1.23. \quad s_-^\dagger = 0.81. \tag{8}$$

Note that because the nature of the caustic entrance is unclear, we report both $s_+^\dagger$ and $s_-^\dagger$. Moreover, because $u_{\rm anom} \sim 0.4$ is large, this is a planetary caustic crossing, so we do not expect a degeneracy in s. Rather, for a major-image caustic, we expect $s \simeq s_+^\dagger$, while for a minor-image caustic, we expect a less precise $s \sim s_-^\dagger$ because the caustic would not lie on the binary axis.

3.3.2. Static Analysis

The grid search returns only one solution, whose refinement is described by the parameters given in Table 3. The heuristic estimate of α proves to be too small by a factor of two relative to the binary axis, i.e., $\alpha - 180^\circ = 8^\circ.1$ versus $18^\circ.9$. This is because the source crosses the binary axis about halfway between the central and planetary caustics, rather than at the planetary caustic. See Figure 3. This, in turn, is partly due to the fact that the planet is relatively massive, $\log q = -2.50$, for which the caustics are offset from the axis by $\eta_{c,-} = 2[q(s^{-2} - 1)]^{1/2} \rightarrow 0.078$ (Han 2006). See Figure 3. Because the caustic entrance is well covered by KMTC data, the normalized source radius, ρ, is determined to better than 10%.

3.3.3. Parallax Analysis

Given the short Einstein timescale $t_{\rm E} \sim 16$ days and the faintness of the source, $I_A \sim 21$, we would not normally expect to be able to measure $\boldsymbol{\pi}_{\rm E}$. Nevertheless, because the event has strong features spread over 6 days, we attempt to do so. Surprisingly, we find a very strong improvement, $\Delta\chi^2 = 116$,

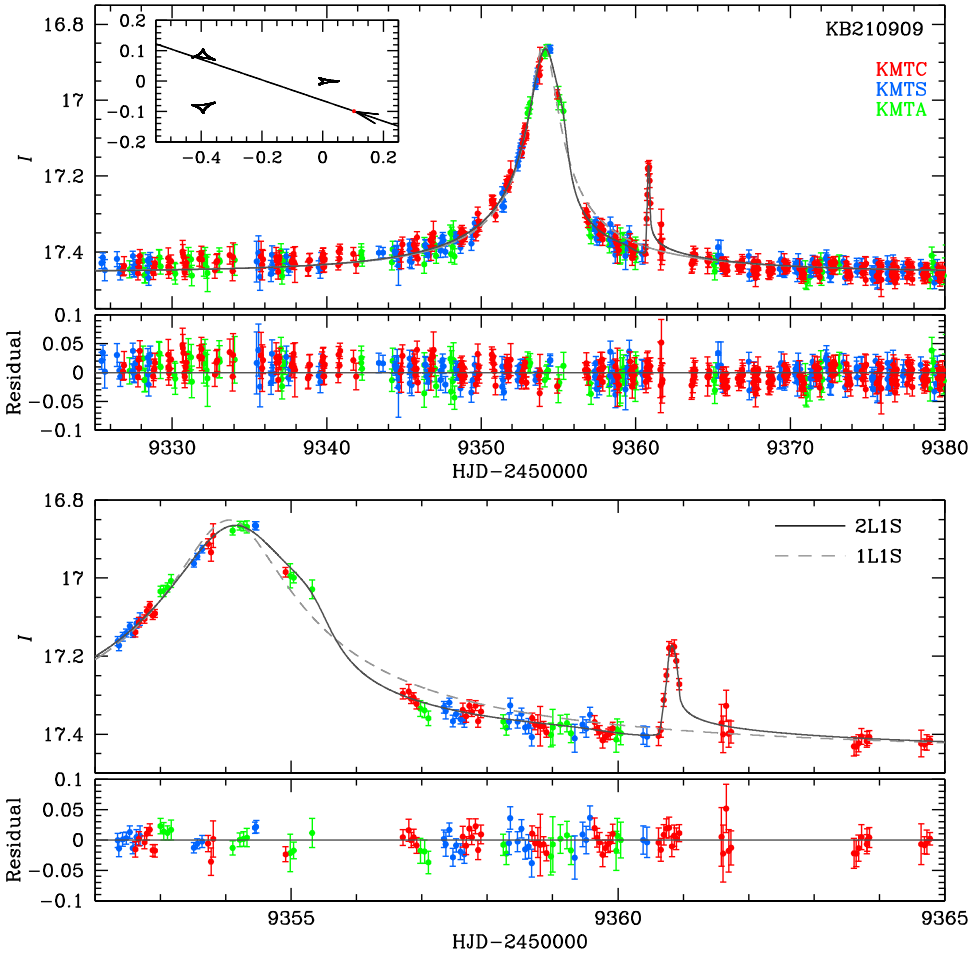

Figure 3. Light-curve data and models for KMT-2021-BLG-0909. Similar to Figure 1, except that the 1L1S model is also shown for comparison. (The data used to create this figure are available.)

Table 3
Microlens Parameters for KMT-2021-BLG-0909

Parameters	2L1S
χ^2/dof	1636.961/1637
$t_0 - 2{,}459{,}350$	4.073 ± 0.017
u_0	0.060 ± 0.004
t_E (days)	16.046 ± 0.733
s	0.823 ± 0.008
q (10^{-3})	3.174 ± 0.446
log q (mean)	-2.497 ± 0.063
α (rad)	3.472 ± 0.012
ρ (10^{-3})	3.326 ± 0.308
I_S [KMTC,pySIS]	20.836 ± 0.060
I_B [KMTC,pySIS]	17.503 ± 0.003
t_{ast} (hr)	1.284 ± 0.085

when the four degrees of freedom (π_E and γ) are added. However, the actual value of the scalar parallax $\pi_E = 20.2 \pm 1.8$ (together with the fit value $\rho = 1.8 \times 10^{-3}$, so $\theta_E \sim 0.67$ mas) would imply a free-floating planet "host" with mass $M_{host} \sim 4.2\,M_J$ orbited by an $M_{planet} = 2.8\,M_\oplus$ "moon," with the system distance being just $D_L = 75$ pc. All of these values are extraordinarily improbable. However, by plotting $\Delta\chi^2 = \chi^2(\text{standard}) - \chi^2(\pi_E, \gamma)$ as a function of time and observatory (not shown), we find that the "signal" comes overwhelmingly from KMTC and that almost none of it comes from the "light-curve features" that originally motivated the parallax fit. We conclude that the parallax signal comes primarily from a low-amplitude (0.03 mag) bump in KMTC near-baseline data, which is almost certainly due to low-level systematics, but when falsely attributed to the 25 times fainter source, it appears as a strong signal. We therefore adopt the standard solution shown in Table 3.

3.3.4. Xallarap Analysis

As a matter of due diligence, we also check whether the light-curve features that were judged to be due to "systematics" in the previous section are, in fact, due to another real physical phenomenon: xallarap. The term "xallarap" refers to light-curve distortions induced by orbital motion of the source around an unseen companion (Griest & Hu 1992; Han & Gould 1997). Xallarap can be an important test of the reality of a parallax signal because any light curve that can be fit by parallax can be fit equally well by xallarap, with source motion parameters that mimic those of Earth. Then, if these xallarap fit parameters do closely mimic Earth's, it would be extraordinarily improbable that these were due to source motion rather than Earth motion, while if they deviated strongly from Earth's parameters, it would be a sign that the light-curve distortion

was mainly due to xallarap or, perhaps, some systematics (Poindexter et al. 2005).

Compared to a standard seven-parameter 2L1S fit, xallarap has five additional parameters (for the simplest xallarap model, i.e., a circular orbit): (P, α_s, δ_s, $\boldsymbol{\xi}$), where $\boldsymbol{\xi} = (\xi_N, \xi_E)$. Here P is the orbital period of the source, $\boldsymbol{\xi}$ is the amplitude and orientation (at t_0) of the source orbit scaled to θ_E, and (α_s, δ_s) give the orientation of the orbital plane, with $90° - \alpha$ being the orbital inclination. This parameterization is chosen so that if the xallarap signal is actually due to parallax, then one will find (within errors) that $P = 1$ yr, $\boldsymbol{\xi} = \boldsymbol{\pi}_E$, and ($\alpha_s$, δ_s) will be the ecliptic coordinates of the event.

We find a best xallarap fit with $P = 0.4$ yr, $\boldsymbol{\xi} = (-1.32, +2.20)$, $(\alpha, \delta) = (190°, 6°)$, and with the other seven parameters being similar to those of the 2L1S standard solution.

From Kepler's third law (and Newton's third law), one finds

$$\frac{Q^3}{(1+Q)^2} = \frac{(a_S/\mathrm{au})^3}{(M_S/M_\odot)(P/\mathrm{yr})^2} \rightarrow 5975, \tag{9}$$

where $Q = M_C/M_S$ is the ratio of the companion mass to that of the source, $a_S = \xi D_S \theta_E = \xi D_S \theta_{\rm ast}/\rho \rightarrow 9.85$ au is the orbital radius of the source, and we have adopted $M_S = 1\,M_\odot$, $D_S = 8$ kpc, $\theta_{\rm ast} = 1.2\,\mu$as from Section 4 and $\rho = 2.5 \times 10^{-3}$ from the xallarap fit. Hence, in this solution, the companion mass would be $M_C = 6000\,M_\odot$. Hence, we reject this solution as spurious, i.e., due to the same systematics that generated the improbable parallax solution.

3.4. KMT-2021-BLG-2478

Figure 4 shows an approximately standard 1L1S light curve with parameters (t_0, u_0, t_E) = (9482.2, 0.08, 43 days), but with two major features superposed: a poorly sampled caustic feature, centered at ∼9486, lasting 1.5–2 days, and a roughly 2-day, roughly symmetric spike, peaking at 9493.9. The sparse coverage is primarily due to the fact that these anomalies occurred near the end of the microlensing season, when the field was visible only about 3 hr per night from each site, and partly due to episodes of adverse weather.

The first (i.e., caustic) structure implies that there must be a second lens. If the system is not more complicated than this, i.e., it is 2L1S, then the presence of two anomalies at $\tau_1 \sim +0.09$ and $\tau_2 \sim +0.29$ after peak almost certainly implies a very large resonant caustic. In principle, however, such multiple anomalies might require more complex systems, such as 3L1S.

3.4.1. Heuristic Analysis

Within the 2L1S framework, $t_{\rm anom} = 9493.9$, i.e., $\tau_{\rm anom} = \tau_2 = 0.27$, and $u_{\rm anom} = 0.29$, so

$$\alpha = 16\overset{\circ}{.}5; \quad s_+^\dagger = 1.16. \tag{10}$$

3.4.2. Static Analysis

The grid search yields only one solution, whose refined parameters are given in Table 4. Note that while the heuristic α prediction was approximately correct, the heuristic $s_+^\dagger$ (combined with $s = 1.055$ from Table 4), predicts a second solution at $s_{\rm inner} = (s_+^\dagger)^2/s_{\rm outer} = 1.28$. Such solutions can generate a cusp-approach spike as the source passes over the ridge between the central and planetary caustics, but the central caustic is not large enough to induce the first caustic anomaly that is seen in the light curve. Hence, there is no degeneracy.

As with KMT-2021-BLG-0909, this planet has a super-Jovian mass ratio.

The Markov Chain Monte Carlo (MCMC) constraints on ρ are not adequately summarized by the median and 68-percentile format of Table 4. In Section 4.3, we will show that the best fit is $\rho \sim 1.1 \times 10^{-3}$ and the 3σ upper limit is $\rho < 1.6 \times 10^{-3}$, while $\theta_{\rm ast} \sim 0.5\,\mu$as. Hence, these ρ values would imply $\theta_E = 0.45$ mas and $\theta_E > 0.3$ mas, respectively. On the other hand, even extremely low values, $\rho \ll 10^{-3}$, are consistent with the data at $\Delta\chi^2 < 5$. Hence, we must at least consider the possibility of very large $\theta_E = \sqrt{\kappa M \pi_{\rm rel}}$ and hence very nearby and/or very massive lenses. The former would imply a large and hence potentially measurable microlens parallax π_E. As mentioned in Section 3.2.2, the complex caustic structure, spanning a significant fraction of t_E, greatly enhances the prospects for making such a measurement.

3.4.3. Parallax Analysis

Including $\boldsymbol{\pi}_E$ and $\boldsymbol{\gamma}$ improves the fit by $\Delta\chi^2 = 64$, with the $u_0 > 0$ and $u_0 < 0$ being almost perfectly degenerate. See Table 4 for the parameters of these fits and Figure 5 for the χ^2 distribution on the $\boldsymbol{\pi}_E$ plane. The most important aspect of these fits is that $\pi_E \sim 0.37 \pm 0.06$ is indeed large, implying $M = \theta_E/\kappa\pi_E \sim 0.18\,M_\odot$ and $D_L = 1/(\pi_E\theta_E + \pi_S) \sim 3.4$ kpc. However, because the errors, particularly in ρ (and hence θ_E), are large, proper estimates will require a Bayesian analysis. See Section 5.3.

3.4.4. 3L1S and 2L2S Analyses

There is no compelling reason to doubt the 2L1S solution: the heuristic analysis based on the second caustic feature approximately predicts the first feature, and the small inconsistency in the static model can be accounted for by reasonable values of $\boldsymbol{\pi}_E$ and $\boldsymbol{\gamma}$. Nevertheless, as a matter of due diligence, we search for solutions in which the second anomaly is due to a second source (2L2S) or second planet (3L1S). However, we do not find any such solutions. The main issue is that models that adequately account for the first anomaly already predict an anomaly at or near the observed incidence of the second anomaly. Hence, we reject such solutions.

3.5. KMT-2021-BLG-1105

Figure 6 shows an otherwise standard 1L1S light curve with parameters (t_0, u_0, t_E) = (9375.8, 0.11, 35 days), punctuated by a sharp spike at $t_{\rm anom} = 9373.4$, i.e., 2.3 days before peak.

3.5.1. Heuristic Analysis

These parameters imply $\tau_{\rm anom} = 0.07$, $u_{\rm anom} = 0.13$, and so

$$\alpha = 122°; \quad s_+^\dagger = 1.067. \tag{11}$$

3.5.2. Static Analysis

Somewhat surprisingly, the grid search returns six local minima. After refinement, we reject two of these because they have high $\Delta\chi^2 = 69$ and 109 and, moreover, have poor fits by eye. However, we briefly note that both have relatively high mass ratios $\log q \sim -1.75$, and for both the spike arises from

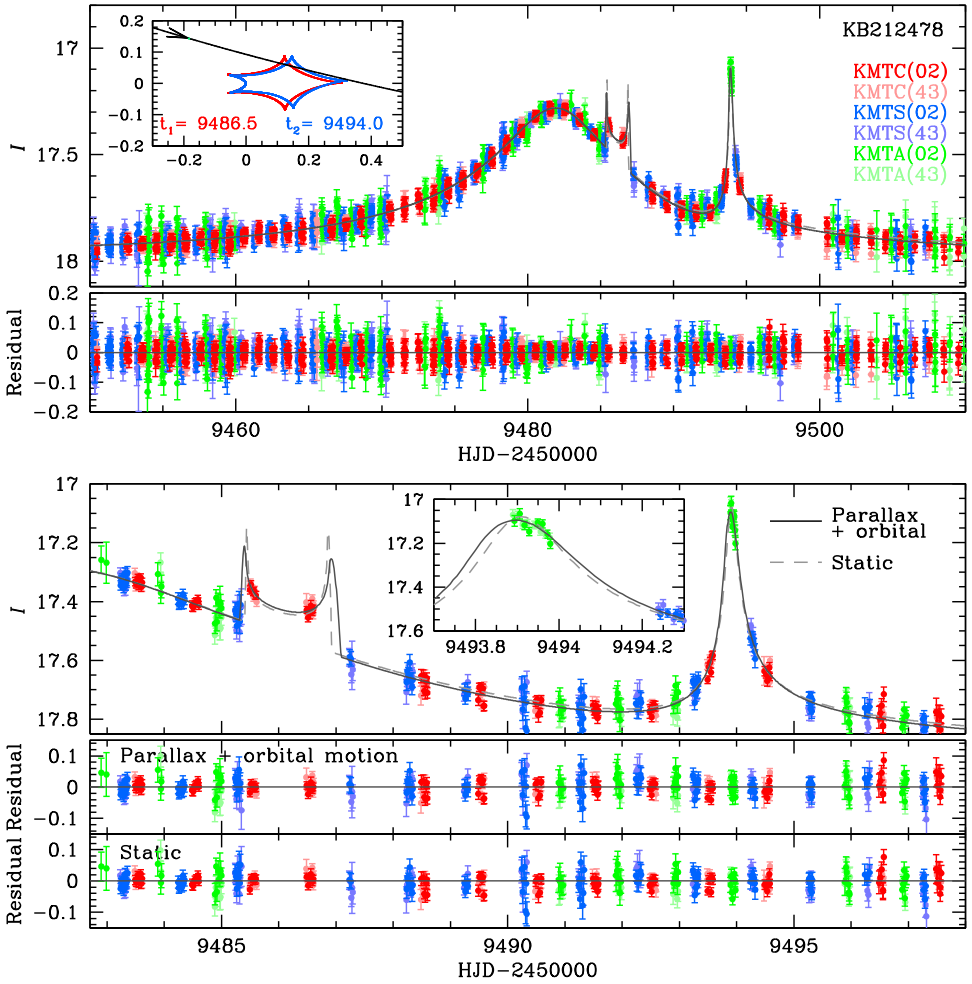

Figure 4. Light-curve data and models for KMT-2021-BLG-2478. The figure is similar to Figure 1, except that the source trajectory inset shows the caustic structure at two epochs and both the static and parallax models are indicated. In addition, there is an inset in the bottom panel that highlights the KMTA coverage of the peak of the "spike."

(The data used to create this figure are available.)

Table 4
Microlens Parameters for KMT-2021-BLG-2478

Parameters	Standard	Parallax + Orbital Motion Models	
		$u_0 > 0$	$u_0 < 0$
χ^2/dof	11327.812/11268	11263.895/11265	11263.879/11265
$t_0 - 2{,}459{,}480$	2.104 ± 0.017	2.162 ± 0.026	2.156 ± 0.026
u_0	0.078 ± 0.001	0.089 ± 0.002	-0.088 ± 0.002
$t_{\rm E}$ (days)	43.111 ± 0.433	37.907 ± 0.660	38.049 ± 0.702
s	1.055 ± 0.001	1.057 ± 0.001	1.056 ± 0.001
q (10^{-3})	3.109 ± 0.101	4.327 ± 0.304	4.206 ± 0.305
log q (mean)	-2.507 ± 0.014	-2.365 ± 0.031	-2.376 ± 0.032
α (rad)	0.276 ± 0.001	0.261 ± 0.010	6.020 ± 0.010
ρ (10^{-4})	4.504 ± 2.262	$8.545^{+2.967}_{-3.938}$	$9.271^{+2.753}_{-3.567}$
$\pi_{{\rm E},N}$	⋯	0.101 ± 0.272	0.078 ± 0.248
$\pi_{{\rm E},E}$	⋯	0.355 ± 0.052	0.339 ± 0.053
ds/dt (yr^{-1})	⋯	0.553 ± 0.120	0.549 ± 0.116
$d\alpha/dt$ (yr^{-1})	⋯	0.589 ± 0.579	-0.113 ± 0.552
I_S [KMTC(01),pySIS]	20.766 ± 0.014	20.607 ± 0.021	20.617 ± 0.022
I_B [KMTC(01),pySIS]	18.063 ± 0.001	18.077 ± 0.002	18.077 ± 0.002
$t_{\rm ast}$ (hr)	0.466 ± 0.235	$0.777^{+0.273}_{-0.359}$	$0.847^{+0.255}_{-0.327}$
β ($\theta_{\rm ast} \equiv 0.5\mu$as)	⋯	$0.226^{+0.203}_{-0.102}$	$0.161^{+0.126}_{-0.069}$

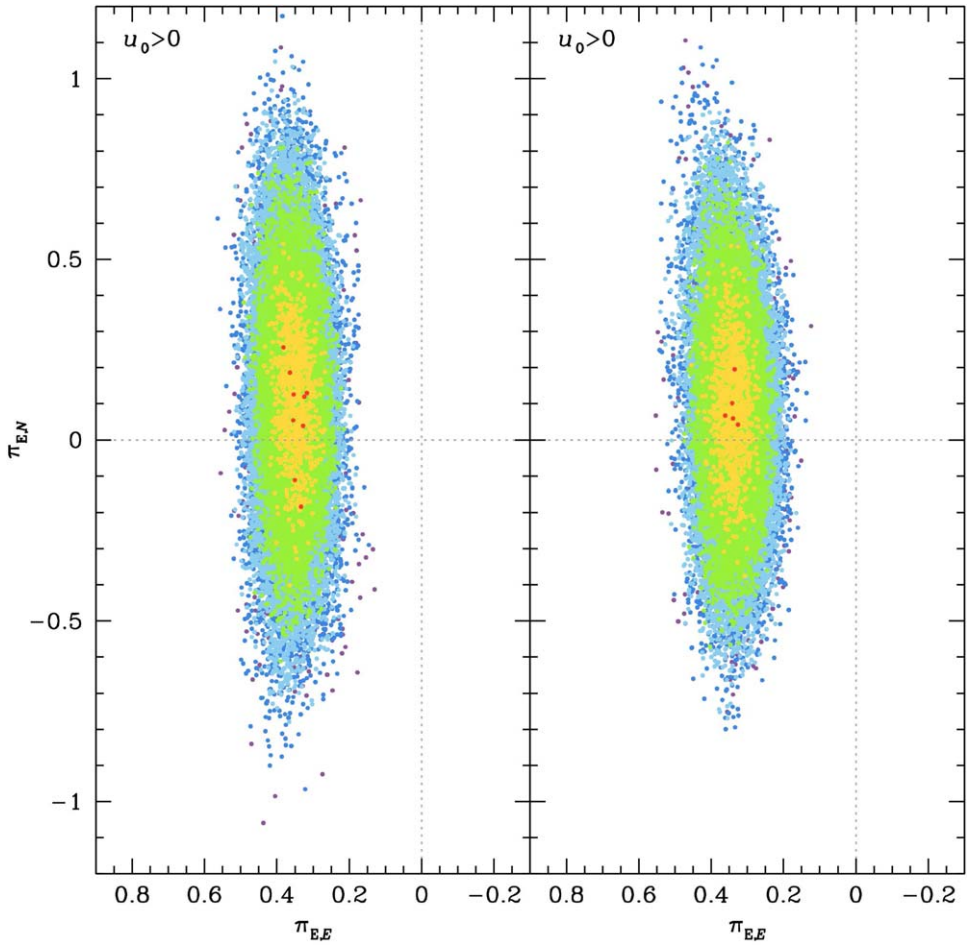

Figure 5. Scatter plot of MCMC trials in the $\boldsymbol{\pi}_E = (\pi_{E,N}, \pi_{E,E})$ plane for the $u_0 > 0$ (left) and $u_0 < 0$ (right) solutions of KMT-2021-BLG-2478. Points are colored (red, yellow, green, cyan, blue) if they are $\Delta\chi^2 <$ (1, 4, 9, 16, 25) from the minimum.

an off-axis cusp approach to a resonant caustic. While these models are certainly not correct, they emphasize the importance of making a systematic search of parameter space because the overall appearance of the models is not qualitatively different from the observed light curve.

The remaining four models are shown in Figure 6, with the corresponding geometries shown in Figure 7, while their refined parameters are given in Table 5. Locals 1 and 2 constitute an inner/outer degeneracy with $s^\dagger = 1.068$, while Locals 3 and 4 constitute a second inner/outer degeneracy with $s^\dagger = 1.066$, both in excellent agreement with Equation (11). This again emphasizes the importance of a systematic search. Because Locals 3 and 4 are each disfavored by $\Delta\chi^2 > 10$, we consider that these solutions are excluded. Nevertheless, it is notable that these two pairs of solutions differ in q by more than a factor of 2.

This is another super-Jovian mass ratio planet, $\log q = -2.7$.

We note that while ρ is not measured, the constraint, $\rho < 0.0013$, at 2.5σ, corresponding to $t_{\rm ast} < 1.1$ hr, is strong enough to play a significant role. That is, in Section 4.4 we will show that $\theta_{\rm ast} = 0.5\ \mu$as, implying $\mu_{\rm rel} = \theta_{\rm ast}/t_{\rm ast} > 4$ mas yr^{-1}, which excludes a significant part of proper-motion parameter space. Hence, when we incorporate the ρ constraint to estimate the physical parameters of the system in Section 5.4, we apply the full $\chi^2(\rho)$ envelope function, rather than a simple limit. For the moment, we simply note that even the 1σ "limit" corresponds to $\mu_{\rm rel} > 6.5$ mas yr^{-1}, and so it still leaves a substantial range of values that are well populated by Galactic models. This fact will become relevant in Section 3.5.3.

Due to the faintness of the source and the lack of complex anomaly structures, we do not attempt a parallax analysis.

3.5.3. Binary–Source Analysis

As with all bump-like anomalies that lack complex or caustic-crossing features, we must check whether the anomaly can be produced by a second source (1L2S) rather than a second lens (2L1S). The results are shown in Table 6.

There are two main features to note about this solution. First, while the χ^2 difference, $\Delta\chi^2 = \chi^2(1L2S) - \chi^2(2L1S) = 5.5$, favors the 2L1S solution, it is not large enough, by itself, to definitively rule out the 1L2S solution.

Second, the value of the second-source self-crossing time, $t_{\rm ast,2} = 1.28$ hr, is well measured in this model (contrary to 2L1S), with just a 5% error. At first sight, this value appears to be very "typical" of historic measurements of $t_{\rm ast}$ for dwarf-star sources in microlensing events. However, in this instance, the source is about 100 times fainter than typical cases, $I_{S,2} = 26.3$. We will show in Section 4.4 that this implies $\theta_{\rm ast,2} = 0.169\ \mu$as and thus $\mu_{\rm rel} = \theta_{\rm ast,2}/t_{\rm ast,2} = 1.16$ mas yr^{-1}. Only a fraction of $p < (\mu_{\rm rel}/\sigma_\mu)^3/6\sqrt{\pi} \rightarrow 0.006$ microlensing events will have such low proper motions (e.g., Gould et al. 2021, 2022a). Here, we have approximated the bulge proper-motion distribution as an isotropic Gaussian, with $\sigma_\mu = 2.9$ mas yr^{-1}. For example, in

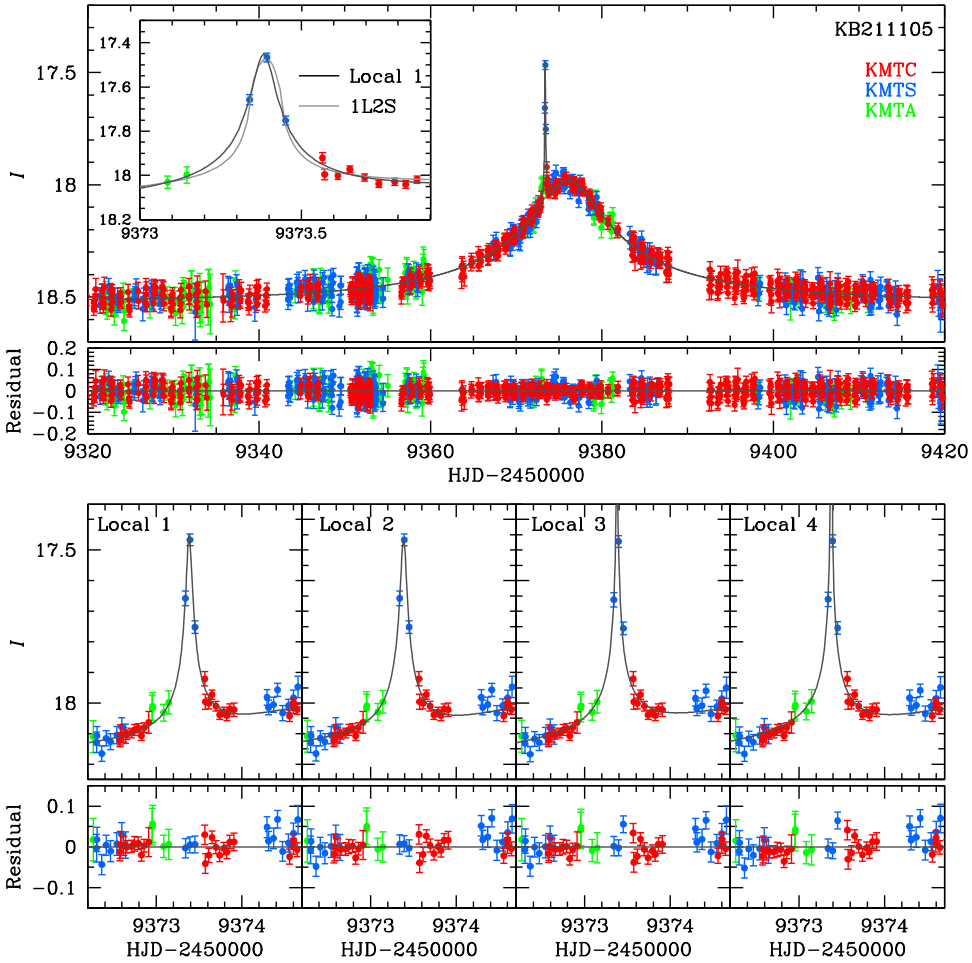

Figure 6. Light-curve data and models for KMT-2021-BLG-1105. Similar to Figure 1, except that the anomaly region is shown in separate panels for the four solutions at the bottom, while the inset at the top compares the 1L2S solution to the Local 1 2L1S solution. In addition, because there are four caustic topologies, these are shown separately in Figure 7.

(The data used to create this figure are available.)

a systematic study of 30 1L1S events with finite-source effects (thus permitting $\mu_{\rm rel}$ measurements), which was sensitive to $\mu_{\rm rel} \geqslant 1.0\,{\rm mas\,yr^{-1}}$, Gould et al. (2022b) found that the slowest (KMT-2019-BLG-0527) had $\mu_{\rm rel} = 1.45\,{\rm mas\,yr^{-1}}$, i.e., $\sigma_\mu/2$. See their Figure 5. Thus, the combination of the $\Delta\chi^2$ preference discussed above with this kinematic argument overwhelmingly favors the 2L1S (i.e., planetary) interpretation.[11]

For completeness, we remark that because the second source would be very red, the 1L2S model predicts that the bump anomaly would be much less pronounced in the V band than the I band. See, e.g., Hwang et al. (2018) for a practical example. Unfortunately, however, there are no V-band data during the anomaly.

Because the interpretation of the event rests heavily on the kinematic argument, we must also consider the possibility that this argument can be evaded (at some cost in χ^2) by solutions with much smaller ρ. We first check that the 1σ error bar on ρ_2 shown in Table 6 is actually representative of the χ^2 surface out to 3σ by fixing ρ_2 at various values. We find that it is. See Table 6 for an example. Next, we search for solutions that are away from this local minimum by enforcing $\rho_2 = 0$. We find that there is such a solution, but it is disfavored by $\Delta\chi^2 = 13.4$. See Table 6. Thus, while this solution avoids the proper-motion constraint, it increases the total χ^2 difference to $\Delta\chi^2 = \chi^2({\rm 1L2S}) - \chi^2({\rm 2L1S}) = 19$. This would be high enough to decisively reject 1L2S were we to adopt the low-ρ_2 solution.

Moreover, there is an additional statistical argument against the 1L2S solution. From the Local 1 panel of Figure 7, it is clear that there is a range of "x," i.e., u_x, of about 0.15 Einstein radii that would generate a qualitatively similar non-caustic-crossing bump. However, the 1L2S solution requires the source to cross the face of the second source, which has a probability of $p = 2\rho_2 \simeq 0.003$, i.e., about 50 times smaller. To fully evaluate this relative probability, we would have to consider

[11] After submission of this paper, Gould (2022) studied an ensemble of 69 KMT planetary events with proper-motion measurements and found that these were much better fit by $d\mu\mu^\nu \exp(-\mu/2\sigma_\mu)^2$ with $\nu \simeq 1$ than the value $\nu = 2$ that is appropriate for the underlying events. See his Figure 7. Gould (2022) suggested that the lower exponent, $\nu = 1$, for planetary events arises because lower proper-motion events evolve more slowly, so the planetary anomalies (with $\Delta\chi^2 \propto \mu^{-1}$) are more easily detected. Presumably, this would apply roughly equally to short (planetary-like) 1L2S anomalies. In this case, the probability derived from the Gould et al. (2021) argument would increase to $p = (\mu/2\sigma_\mu)^{\nu+1}/[(\nu+1)/2]! \rightarrow (\mu/\sigma_\mu)^2/4$, i.e., $p = 0.04$ in the present case. When combined with the fact that 1L2S is disfavored by $\Delta\chi^2 = 5.5$, this is still sufficient to confidently exclude the 1L2S solution.

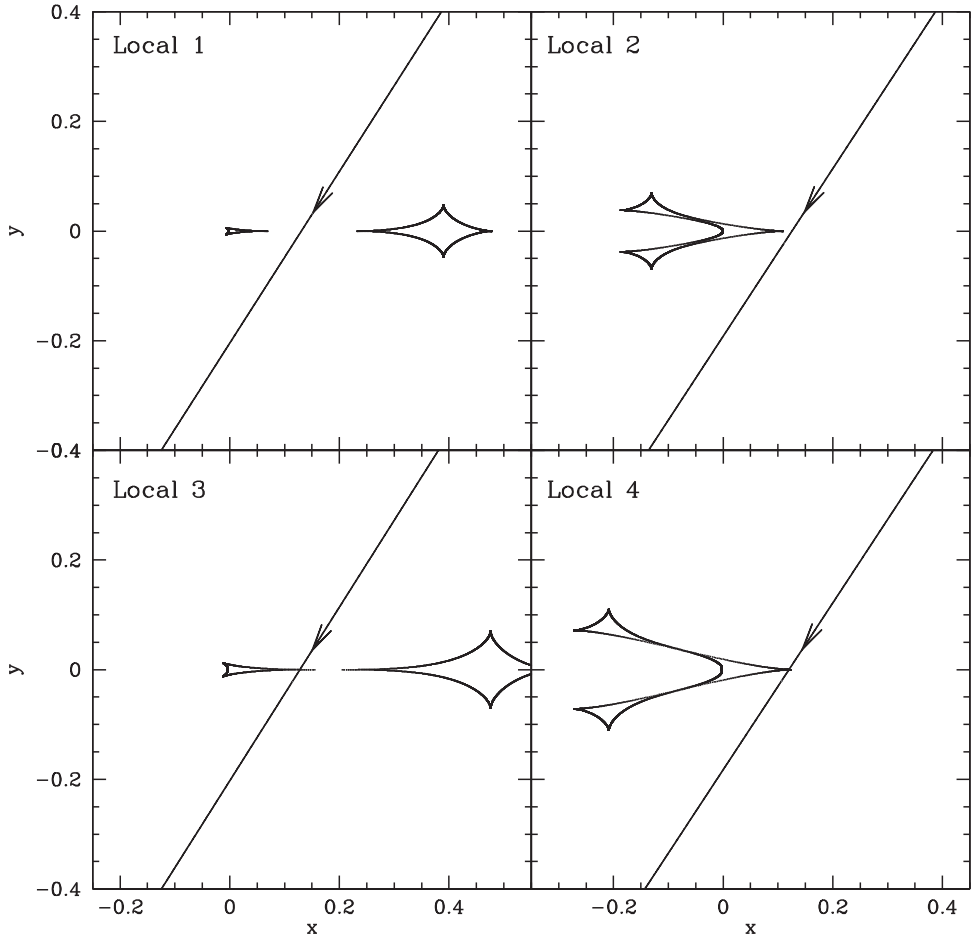

Figure 7. Caustic topologies and source trajectories for each of the four solutions of KMT-2021-BLG-1105. Locals 1 and 2 constitute an "inner/outer" degenerate pair satisfying $s_+^\dagger \simeq s^\dagger \equiv \sqrt{s_{\rm inner} s_{\rm outer}}$ to high precision (Equation (11)), while Locals 3 and 4 constitute a second such pair that satisfy this equation equally well. The first pair are ridge crossing, while the second pair are cusp crossing. The first pair are favored by $\Delta\chi^2 > 10$ and hence are adopted here.

Table 5
Microlens Parameters for KMT-2021-BLG-1105

Parameters	Local 1	Local 2	Local 3	Local 4
χ^2/dof	1784.854/1785	1788.955/1785	1795.837/1785	1806.507/1785
$t_0 - 2{,}459{,}370$	5.826 ± 0.036	5.856 ± 0.036	5.711 ± 0.036	5.780 ± 0.035
u_0	0.109 ± 0.007	0.107 ± 0.007	0.107 ± 0.007	0.101 ± 0.005
$t_{\rm E}$ (days)	34.965 ± 1.919	$35.374^{+2.264}_{-1.739}$	34.425 ± 1.985	$36.248^{+1.887}_{-1.488}$
s	1.214 ± 0.008	0.939 ± 0.008	1.265 ± 0.013	0.899 ± 0.010
q (10^{-3})	1.984 ± 0.200	1.934 ± 0.191	4.939 ± 0.694	4.573 ± 0.614
log q (mean)	-2.703 ± 0.044	-2.714 ± 0.043	-2.308 ± 0.062	-2.341 ± 0.058
α (rad)	2.140 ± 0.009	2.148 ± 0.010	2.136 ± 0.010	2.152 ± 0.009
ρ (10^{-3})	<1.3	<1.3	<1.3	<1.3
I_S [KMTC,pySIS]	21.233 ± 0.074	$21.258^{+0.085}_{-0.070}$	21.207 ± 0.080	21.294 ± 0.062
I_B [KMTC,pySIS]	18.614 ± 0.006	18.612 ± 0.006	18.616 ± 0.006	18.609 ± 0.004
$t_{\rm ast}$ (hr)	<1.1	<1.1	<1.1	<1.1

the relative probabilities of the presence of a lens planetary companion, compared to a source M-dwarf companion, which we do not attempt here because it is unnecessary to make the basic argument. Nevertheless, it is clear that the 1L2S solution requires some fine-tuning.

While we cannot absolutely rule out the 1L2S solution, the formal probability that it is correct is about $p \sim 1/400$. Hence, this planet should be accepted as genuine. We note that its reality can be definitively tested at first adaptive optics (AO) light on next-generation (30 m) telescopes, roughly in 2030, i.e., $\Delta t = 9$ yr after the event. If, as anticipated, the 2L1S model is correct, then the source and lens will be separated by $\Delta\theta = \mu_{\rm rel}\Delta t \gtrsim 36$ mas, so they will be easily resolved. On the other hand, if the 1L2S model were correct, then the separation would be $\Delta\theta \sim 9\,{\rm mas\,yr^{-1}}$, which would probably be too small to resolve, but even if resolved, it would provide a measurement that was consistent with 1L2S but not with 2L1S.

Before leaving the issue of 1L2S models, we note that, as a matter of "due diligence," we explored 1L2S models in which finite-source effects were permitted for both the primary and

Table 6
1L2S for KMT-2021-BLG-1105

Parameters	1L2S	$\rho_2 = 0.001$	$\rho_2 = 0.0$
χ^2/dof	1790.359/1785	1800.137/1786	1803.805/1786
$t_{0,1} - 2459370$	6.162 ± 0.041	6.151 ± 0.041	6.192 ± 0.043
$u_{0,1}$	0.105 ± 0.010	$0.077^{+0.007}_{-0.005}$	0.103 ± 0.010
t_E (days)	37.787 ± 3.115	49.293 ± 3.400	38.450 ± 3.202
$t_{0,2} - 2459370$	3.389 ± 0.002	$3.388^{+0.003}_{-0.004}$	3.381 ± 0.004
$u_{0,2}$ (10^{-3})	0.000 ± 0.313	0.025 ± 0.322	0.654 ± 0.101
ρ_2 (10^{-3})	1.416 ± 0.139	1	⋯
q_F (10^{-2})	1.021 ± 0.055	1.065 ± 0.072	1.186 ± 0.088
I_S [KMTC,pySIS]	21.355 ± 0.113	$21.703^{+0.080}_{-0.098}$	21.381 ± 0.113
I_B [KMTC,pySIS]	18.605 ± 0.007	$18.586^{+0.005}_{-0.003}$	18.603 ± 0.007
$I_{S,2}$ [KMTC,pySIS]	26.344 ± 0.103	$26.657^{+0.065}_{-0.106}$	26.211 ± 0.111
$t_{ast,2}$ (hr)	1.284 ± 0.068	1.183 ± 0.082	⋯

secondary sources, even though such effects are extremely unlikely for the primary, a priori, because $t_{\rm eff} \equiv u_0 t_E \sim 4$ days is extremely long relative to the typical self-crossing time of dwarf stars, $t_{\rm ast} \sim 1$ hr. Surprisingly, we did indeed find such solutions with $\Delta\chi^2 \sim -6$ relative to the solution reported in Table 6 (and hence comparable χ^2 to the 2L1S solution). However, these had $(\rho_1, \rho_2) \simeq (0.2, 0.002)$, which would imply grossly inconsistent estimates for $\theta_E = \theta_{\rm ast}/\rho$ of 2.5 μas versus 85 μas. Hence, it is unphysical. The χ^2 improvement could be a purely statistical fluctuation ($p = 0.05$), or it could be due to low-level systematics in the photometry. In any case, we reject this solution.

Finally, we remark that this event was included in the present study only because our "mass production" project aims to document all 2021 events with viable planetary solutions, in the spirit pioneered by Gould et al. (2022a) and Jung et al. (2022) for 2018 events, irrespective of whether such planetary solutions are decisively preferred. Our initial assessment, based on detailed modeling of TLC reductions, was that its interpretation was ambiguous, and thus it would not enter planetary catalogs. It was only in the course of comprehensively evaluating all the evidence that we concluded that the planetary solution is decisively favored.

4. Source Properties

Our evaluation of the source properties exactly follows the goals and procedures of Paper I. In this introduction, we repeat only the most essential descriptions from Section 4 of that work, in particular (as in Section 3.1) documenting all notation.

We analyze the color–magnitude diagram (CMD) of each event, primarily to measure $\theta_{\rm ast}$ and so to determine

$$\theta_E = \frac{\theta_{\rm ast}}{\rho}; \quad \mu_{\rm rel} = \frac{\theta_E}{t_E}. \tag{12}$$

We follow the method of Yoo et al. (2004). We first find the offset of the source from the red clump

$$\Delta[(V-I), I] = [(V-I), I]_S - [(V-I), I]_{\rm cl}. \tag{13}$$

We adopt $(V-I)_{\rm cl,0} = 1.06$ from Bensby et al. (2013) and evaluate $I_{\rm cl,0}$ from Table 1 of Nataf et al. (2013), based on the Galactic longitude of the event, which yields the dereddened color and magnitude of the source,

$$[(V-I), I]_{S,0} = [(V-I), I]_{\rm cl,0} + \Delta[(V-I), I]. \tag{14}$$

Next, we transform from V/I to V/K using the *VIK* color–color relations of Bessell & Brett (1988), and we apply the color/surface brightness relations of Kervella et al. (2004) to obtain $\theta_{\rm ast}$. After propagating the measurement errors, we add 5% to the error in quadrature to take account of systematic errors due to the method as a whole.

To obtain $[(V-I), I]_S$, we always begin with pyDIA reductions (Albrow 2017), which put the light curve and field-star photometry on the same system. With one exception (see below), we determine $(V-I)_S$ by regression of the V-band data on the I-band data, and we determine I_S by regression of the I-band data on the best-fit model. For two of the four events analyzed in this paper, there is calibrated OGLE-III field-star photometry (Szymański et al. 2011). For these two cases, we transform $[(V-I), I]_S$ to the OGLE-III system. For the two remaining cases, we work in the instrumental KMT pyDIA system.

For KMT-2021-BLG-0909, the source is too faint in the V band to measure the source color from the light curve. We therefore employ a different technique, as described in Section 4.2.

The CMDs are shown in Figure 8.

The elements of these calculations are summarized in Table 7. In all cases, the source flux is that of the best solution. Under the assumption of fixed source color, $\theta_{\rm ast}$ scales as $10^{-\Delta I_S/5}$ for the other solutions, where ΔI_S is the difference in source magnitudes, as given in the tables of Section 3. The inferred values (or limits upon) θ_E and $\mu_{\rm rel}$ are given in the individual event subsections below, where we also discuss other issues, when relevant.

4.1. KMT-2021-BLG-0712

There are two issues related to the source that require some care for this event. First, the source color shown in Table 7, $(V-I)_{S,0} = 0.69 \pm 0.06$, is unusually blue given that the source lies $\Delta I = 5.9$ mag below the clump. If the source were a typical bulge star of this brightness, we would expect $(V-I)_{S,0} \sim 1.1$, based on Hubble Space Telescope (HST) images of Baade's window taken by Holtzman et al. (1998). Logically, there are three possibilities: our color measurement is incorrect, the source lies well behind the bulge and thus is much more luminous (and so bluer) than a bulge star of similar brightness, or the source is atypical, e.g., has much lower metallicity than typical bulge stars. The first of these explanations is the only one of direct concern here: if the color and magnitude of the source are correctly measured, regardless of the exact cause of it being so blue, then the derived $\theta_{\rm ast}$ will also be correct.

We therefore check the color determination as follows: The color and magnitude reported in Table 7 are based on the KMTC41 data set. We repeat the calculation using the KMTC01 data set, which is composed of a completely independent series of observations. While these observations are made with the same (KMTC) telescope, the observational times are different, and the positions on the focal plane are offset by 8′. However, the best-fit color is the same to within 0.01 mag. Neither of the other two explanations appears likely a priori. To be sufficiently more luminous to account for the color discrepancy, the source should be roughly a factor of 2 more distant than the bulge, which would place it almost 1 kpc below the Galactic plane. While there are certainly some stars at this height and this Galactocentric radius (i.e., similar to that

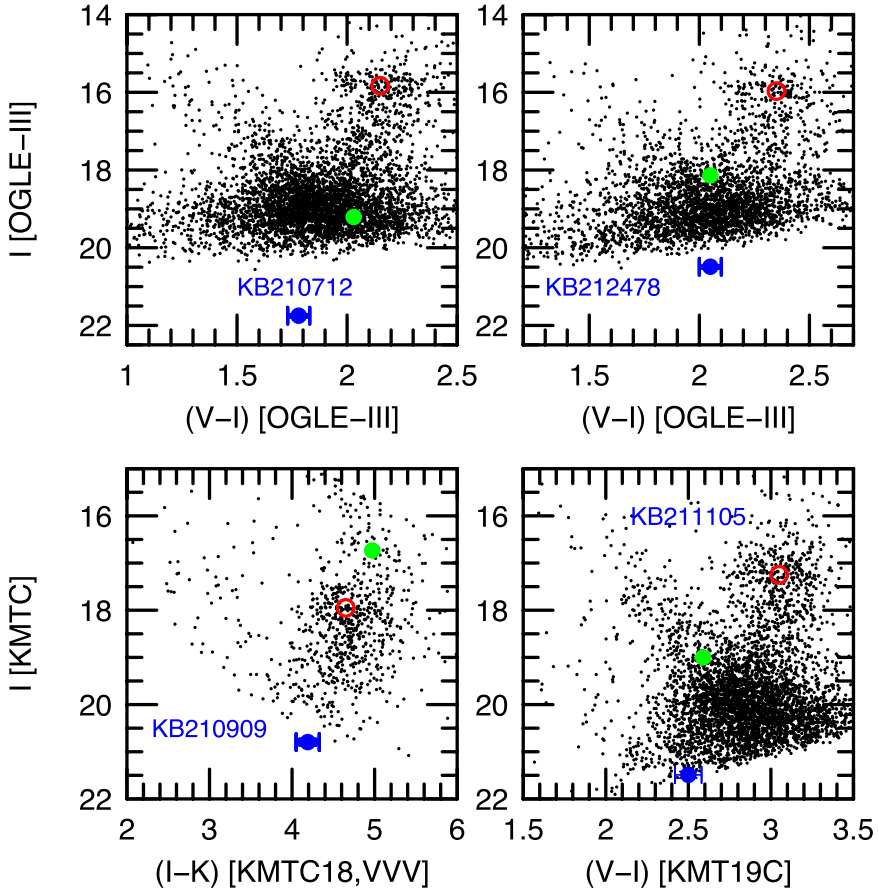

Figure 8. CMDs for each of the four planets reported here. The source positions (blue) and clump-giant centroids (red) are shown for all events. Where relevant, the blended light is shown in green.

Table 7
CMD Parameters for Four 2021 Planets

Parameter	KB210712	KB210909	KB212478	KB211105
$(V-I)_S$	1.78 ± 0.05	N.A.	2.05 ± 0.05	2.50 ± 0.08
$(V-I)_{\rm cl}$	2.15 ± 0.03	N.A.	2.35 ± 0.03	3.05 ± 0.04
$(V-I)_{\rm cl,0}$	1.06	1.06	1.06	1.06
$(V-I)_{S,0}$	0.69 ± 0.06	0.81 ± 0.08	0.76 ± 0.06	0.51 ± 0.09
I_S	21.75 ± 0.02	20.80 ± 0.06	20.49 ± 0.03	21.49 ± 0.07
$I_{\rm cl}$	15.83 ± 0.05	17.95 ± 0.05	15.97 ± 0.05	17.25 ± 0.05
$I_{\rm cl,0}$	14.48	14.41	14.39	14.37
$I_{S,0}$	20.40 ± 0.06	17.26 ± 0.08	19.09 ± 0.06	18.61 ± 0.09
$\theta_{\rm ast}$ (μas)	0.255 ± 0.023	1.205 ± 0.163	0.504 ± 0.042	0.482 ± 0.053

Note. Event names are abbreviations, e.g., KMT-2021-BLG-0712. $[(V-I), I]_S$ and $[(V-I), I]_{\rm cl}$ for KB210712 and KB212478 are based on calibrated OGLE-III photometry, while the other two events have instrumental KMT photometry.

of the Sun), they are relatively rare. Extremely metal-poor stars in the bulge are likewise rare.

Despite the low prior likelihood of either of these two options, they are not unphysical, and hence we adopt the measured color, and hence the value of $\theta_{\rm ast} = 0.255\ \mu$as given in Table 7, and we thereby derive

$$\theta_{\rm E} = 0.604 \pm 0.095\ {\rm mas}; \quad \mu_{\rm rel} = 2.19 \pm 0.34\ {\rm mas\ yr^{-1}}, \times (u_0 < 0) \tag{15}$$

and

$$\theta_{\rm E} = 0.636 \pm 0.091\ {\rm mas}; \quad \mu_{\rm rel} = 2.62 \pm 0.37\ {\rm mas\ yr^{-1}}, \times (u_0 > 0). \tag{16}$$

The second issue that requires some care is the location of the blend relative to the source. If these were closely aligned, it would argue for the blend being associated with the event, being either the lens itself or a companion to the lens or the source.

In the KMTC41 pyDIA analysis, the baseline object appears to lie $\Delta\boldsymbol{\theta}(N, E) = (170, 145)$ mas northeast of the source. The issue that requires care is that there is another, slightly brighter star that lies 1″ northwest of the baseline object, which could in principle corrupt the astrometry of the baseline object. (The position of the source is determined from difference images, for which no such issues arise.) We conduct two tests. First, we repeat the analysis using the KMTC01 observations and find almost exactly the same result. Second, we find, after transforming coordinates to the OGLE-III system, that the offset is qualitatively similar: $\Delta\boldsymbol{\theta}(N, E) = (80, 250)$ mas. Note that because the epoch of the OGLE-III data is 15 yr earlier, we expect offsets of order 50 mas in each direction, in addition to normal measurement errors. The blend is 0.12 mag bluer and 3.38 mag fainter than the clump (see Figure 8), and it is therefore likely to be a bulge subgiant. We conclude that it is most likely not related to the event. The lens must be fainter than the blend, but because the two are separated by just 220 mas, we cannot place more stringent constraints on the lens light than this.

4.2. KMT-2021-BLG-0909

Due to high extinction, $A_I \sim 4$, the source is too faint in the V band to measure the source color from the light curve. In such cases, one generally estimates the source color based on its offset in the I band from the centroid of the red clump. As often happens for such heavily reddened fields, it is difficult to precisely locate the red clump on the pyDIA (or, when available, OGLE-III) CMD because even red clump stars are near or below the measurement threshold in the V band. In the present case, we find that the red clump is detectable on the pyDIA CMD, but its centroid cannot be reliably determined because the lower part of the clump merges into the background noise of the diagram.

Therefore, we measure the clump centroid on an $[(I-K), I]$ CMD, which we construct by matching pyDIA I-band photometry with K-band photometry from the VVV catalog (Minniti et al. 2017). See Figure 8. To estimate the color, we first find the offset from the clump $\Delta I = I_S - I_{\rm cl} = 2.85 \pm 0.08$. See Table 7. If the source were exactly at the mean distance of the clump, it would therefore have an absolute magnitude, $M_I = 2.73$. In fact, it is more likely to be toward the back of the bulge (because it must be behind the lens), so a plausible range of possibilities is $2.2 \lesssim M_I \lesssim 2.9$. In this range, the source could be almost anywhere along the turnoff/subgiant branch. To account for this, we adopt a uniform distribution, $0.60 < (V-I)_{S,0} < 1.00$, which we summarize as a 1σ range of $(V-I)_{S,0} = 0.80 \pm 0.12$. This source position is illustrated in Figure 8 by transforming from $(V-I)$ to $(I-K)$ using the relations of Bessell & Brett (1988). These values lead to estimates of

$$\theta_{\rm E} = 0.362 \pm 0.049 \ {\rm mas}; \quad \mu_{\rm rel} = 8.24 \pm 1.11 \ {\rm mas\ yr^{-1}}. \quad (17)$$

Also shown in the CMD is the position of the blended light, which is a bright giant that is more than 1 mag above the clump. We find that this star is displaced by 0.″73 from the source toward the southwest. This bright star is almost certainly not associated with the event, but it prevents us from placing any useful limits on the lens light.

For completeness, we note that the coordinates shown for this event in Table 1 are, as usual, those of the nearest catalog star, namely the bright giant just discussed. However, these differ from the coordinates shown on the KMT web page, which are about 1.″5 yet farther south. When the event was originally triggered by AlertFinder (Kim et al. 2018b), it was identified with this more southerly catalog star. One day later, it was again triggered, this time by the closer (bright) catalog star, but our standard procedures enforce maintaining the coordinates of the original announcement on the web page to avoid confusion.

4.3. KMT-2021-BLG-2478

The source star, whose parameters are given in Table 7 and whose CMD position is shown in Figure 8, lies 4.5 mag below the clump and is about 0.07 ± 0.06 mag redder than the Sun. That is, it is a bulge mid-G dwarf. Unfortunately, as discussed in Section 3.4, we have only a χ^2-envelope constraint on ρ, rather than a precise measurement. See Figure 9. For the present, we therefore give the estimates of $\theta_{\rm E}$ and $\mu_{\rm rel}$ scaled to that section's best estimate,

$$\theta_{\rm E} = \frac{1.1 \times 10^{-3}}{\rho}(0.45 \pm 0.04) \ {\rm mas}$$
$$\mu_{\rm rel} = \frac{1.1 \times 10^{-3}}{\rho}(4.3 \pm 0.4) \ {\rm mas\ yr^{-1}}. \quad (18)$$

Figure 8 shows the location of the blended light, which is 2.35 mag brighter than the source and of similar color. We find that the source is displaced from the baseline object by $\Delta\theta = 220$ mas to the southeast. It is consistent with being a bulge turnoff/subgiant star and thus could in principle be a companion to the source, but there is no strong evidence in favor of this hypothesis. In Section 5.3, we will impose the constraint on lens light: $I_L > I_B$.

4.4. KMT-2021-BLG-1105

As shown in Table 7, the source star lies 4.24 mag below the clump and is measured to have $(V-I)_{S,0} = 0.51 \pm 0.09$. This is unexpectedly blue, although it is within 1σ of a plausible value for a relatively metal-poor turnoff star. We attempt to check this measurement using KMTS data. However, these have too few magnified V-band points for a reliable measurement. We adopt the orientation that our normal error estimates adequately cover the measurement uncertainty. As discussed in Section 3.5, we obtain only a $\chi^2(\rho)$ envelope function, which we will incorporate into the Bayesian analysis in Section 5.4. See Figure 10. Hence, the $\theta_{\rm ast}$ determination in Table 7 does not lead to unambiguous estimates of $\theta_{\rm E}$ and $\mu_{\rm rel}$. These can be fully investigated only in the context of the Bayesian analysis. For the moment, we express them in parametric form,

$$\theta_{\rm E} = \frac{8.2 \times 10^{-4}}{\rho} \times (0.59 \pm 0.07) \ {\rm mas};$$
$$\mu_{\rm rel} = \frac{8.2 \times 10^{-4}}{\rho} \times (6.1 \pm 0.7) \ {\rm mas\ yr^{-1}}, \quad (19)$$

where the prefactor has values $\simeq(1, 0.71, 0.57)$ at $\Delta\chi^2 = (1, 4, 9)$ of the envelope function. Thus, in contrast to many cases that lack a clear ρ measurement, the ρ constraint will play a significant role.

As also discussed in Section 3.5, evaluating the angular radius of the second source in the 1L2S solution, $\theta_{\rm ast,2}$, is

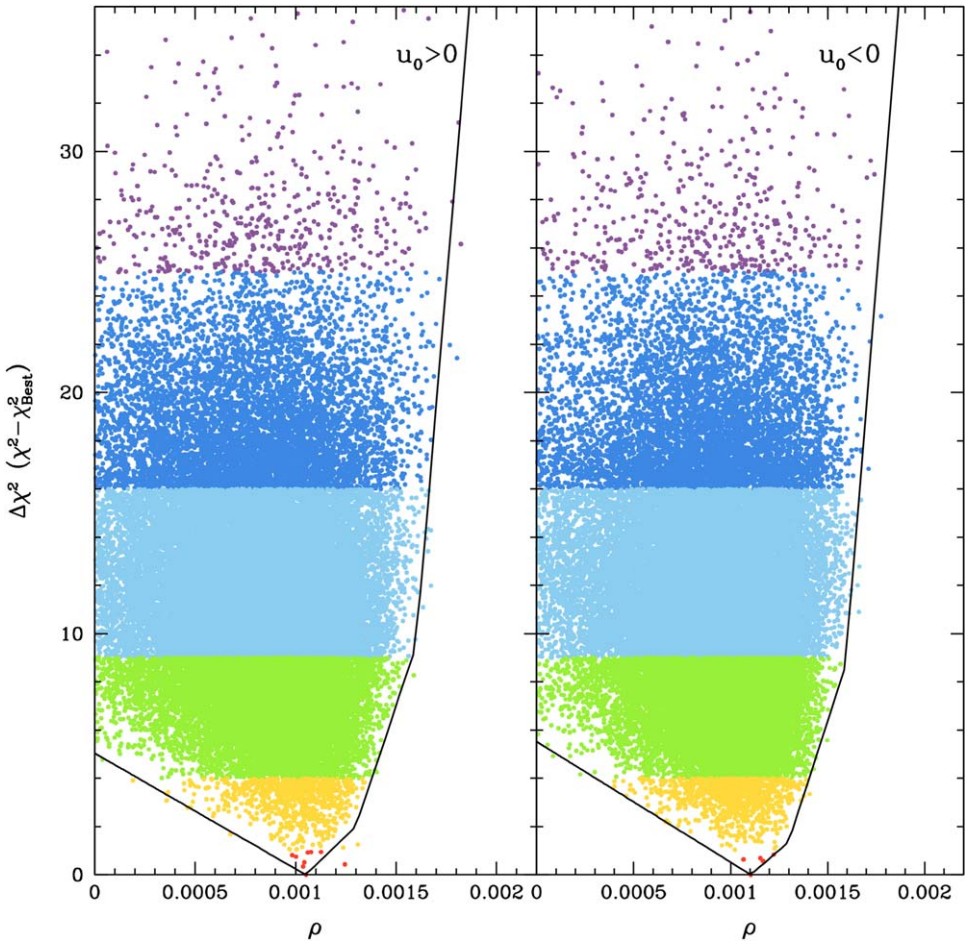

Figure 9. Envelope function (solid curve) of $\Delta\chi^2(\rho)$ derived from the lower limit of MCMC trials (colored points) for KMT-2021-BLG-2478.

critically important to the kinematic argument against this solution. We present a new method for doing so, which is particularly adapted to mid- to late M dwarfs, for which it may be very difficult to make the color measurements that are needed for the traditional (Yoo et al. 2004) method. The first step is to note, from Tables 5 and 6, that this second source is 5.11 mag fainter than the source in the Local 1 2L1S model, which (from Table 7) is 4.22 mag fainter than the clump. That is, the second source is 9.33 ± 0.11 mag fainter than the clump, where the error is the quadrature sum of the errors in $I_{S,2}$ (Table 6) and $I_{\rm cl}$ (Table 7). We adopt $I_{\rm cl,0} = 14.37$ and $M_{I,\rm cl} = -0.12$.

We do not know, a priori, the exact distance of the source system along the line of sight. As noted above, the primary source appears to be a bulge turnoff star and so could in principle be anywhere in the bulge. We will consider below the full range of distances, but for the moment we adopt a fiducial distance modulus $\mathrm{Dmod_{fid}} = 14.37 - (-0.12) + 0.2 = 14.69$, i.e., 0.2 mag behind the clump centroid.

Next, we evaluate the second-source radius under the assumption that it lies exactly at this distance, and we initially ignore the error in its flux measurement. That is, we initially assume that it has an absolute magnitude $M_{I,2} = 9.33 + (-0.12) - 0.20 = 9.01$. Using the mass–luminosity relations of Benedict et al. (2016) in V and K, together with the VIK color–color relations of Bessell & Brett (1988), we find that the mass of the putative second source would be $M_{S,2} = 0.314\,M_\odot$. We then adopt the M-dwarf mass–radius relation $(R/R_\odot) = (M/M_\odot)$ from Figure 7 of Parsons et al. (2018) and so obtain $R_2 = 0.314\,R_\odot$ and thus $\theta_{\rm ast,2} = 0.169\,\mu$as.

We now take account of the fact that the source system could be at other distance moduli in the bulge. For example, if it were at 0.1 mag larger Dmod, then it would likewise be 0.1 mag more luminous, and so would have correspondingly larger mass (and radius), but the impact of this larger physical size on $\theta_{\rm ast,2}$ would be countered by the larger distance of the system. Applying the above arguments to arbitrary distances (within the bulge), we find $dM_I/d\ln M = -2.430$, and so (after a few steps)

$$\theta_{\rm ast,2} = 0.169\ \mu\mathrm{as} \times 10^{-0.0213\ \Delta\mathrm{Dmod}}, \qquad (20)$$

where ΔDmod is the difference between the true distance modulus and the fiducial one adopted above. Stated alternatively, $\theta_{\rm ast,2} \propto D_S^{0.046}$. Thus, for example, if we adopt $\Delta\mathrm{Dmod} = 0 \pm 0.3$, then (still not taking account of the measurement error of $\sigma(I_{s,2}) = 0.11$) we find $\theta_{\rm ast,2} = 0.169 \pm 0.003\,\mu$as. The main error then comes from this measurement error, $\sigma(\ln\theta_{\rm ast}) = 0.11/2.43 = 0.045$. This leads to $\mu_{\rm rel} = 1.16 \pm 0.08\ \mathrm{mas\ yr^{-1}}$, which we argued in Section 3.5.3 is highly unlikely.

Finally, the blended light lies on the foreground main sequence of the CMD in Figure 8. In principle, it might therefore be the lens or a companion to the lens. We therefore carefully investigate the offset between the magnified source and the baseline object $\Delta\boldsymbol{\theta}(N, E) = \boldsymbol{\theta}_{\rm base} - \boldsymbol{\theta}_S$. We make four

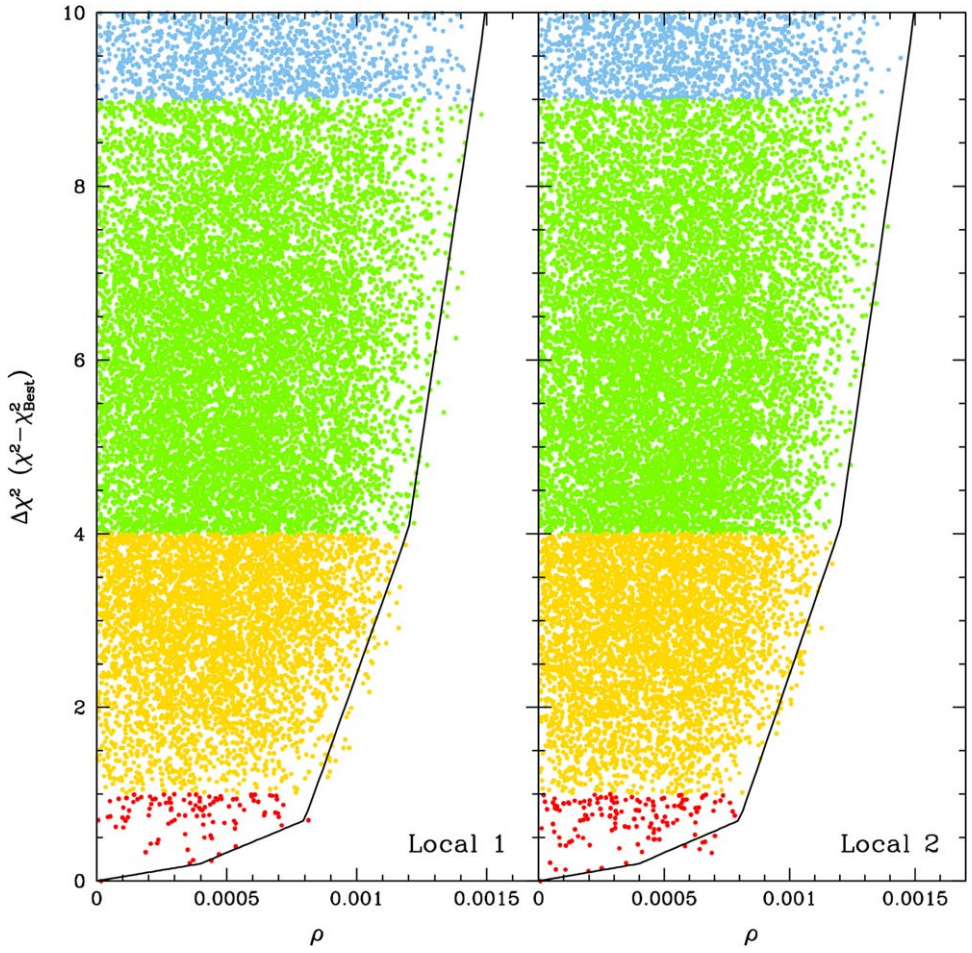

Figure 10. Envelope function (solid curve) of $\Delta\chi^2(\rho)$ derived from the lower limit of MCMC trials (colored points) for KMT-2021-BLG-1105.

measurements by applying two independent algorithms (pyDIA and pySIS) to two independent data sets (KMTC and KMTS). The best-fit values of the measurements are (in mas) $\Delta\boldsymbol{\theta}_{\rm KMTC,pyDIA} = (+80, +72)$, $\Delta\boldsymbol{\theta}_{\rm KMTS,pyDIA} = (+59, +24)$, $\Delta\boldsymbol{\theta}_{\rm KMTC,pySIS} = (+61, +78)$, and $\Delta\boldsymbol{\theta}_{\rm KMTS,pySIS} = (+106, +142)$.

Before investigating the issue of measurement errors, we note that three of the four measurements lead to $|\Delta\boldsymbol{\theta}| \lesssim 0.''1$. The surface density of foreground-main-sequence stars that are brighter than the blend is just 39 arcmin^{-2}, implying that the probability for a random field star to lie within $0.''1$ is just $p = 3.4 \times 10^{-4}$. Thus, we must seriously consider the possibility that the apparent offset is due to measurement error.

The offset measurements have two sources of error: the error in the source position (derived from difference images), and the error in the baseline-object position (derived from point-spread function (PSF) photometry/astrometry of the baseline images). We expect the first of these to be small because the difference images are virtually free of systematic structures, apart from the magnified source. For example, in the two pySIS analyses, we find standard deviations from the six magnified images to be (again in mas) $\sigma_{\rm KMTC} = (21, 22)$ and $\sigma_{\rm KMTS} = (50, 25)$. The scatter is substantially smaller than the offsets, and it is plausible to treat these six measurements as independent, in which case the standard errors of the mean are substantially smaller yet.

However, it is substantially more difficult to estimate the errors in the DoPhot (Schechter et al. 1993) PSF-photometry measurement of the baseline-object position. While the baseline object appears isolated on the image, and the nearest neighbor in the star catalog is separated from the baseline object by $1.''1$, the astrometry of the baseline object could easily be corrupted by a faint field star. For example, an $I = 20.75$ star separated by $0.''5$ would not be separately resolved and would generate $0.''1$ error in the measured position. The surface density of such stars (without accounting for incompleteness at these faint magnitudes) is 608 arcmin^{-2}, implying that the expected number within $0.''5$ is $p = 13\%$. Therefore, it is quite plausible that the blended light is primarily due to the lens or a companion to the lens, although the evidence in favor of this scenario is certainly not definitive. We discuss the implications of this further in Section 5.4.

5. Physical Parameters

None of the four planets have sufficient information to precisely specify the host mass and distance. Moreover, several have multiple solutions with significantly different mass ratios q and/or different Einstein radii $\theta_{\rm E}$. For any given solution, we can incorporate Galactic-model priors into standard Bayesian techniques to obtain estimates of the host mass $M_{\rm host}$ and distance D_L, as well as the planet mass $M_{\rm planet}$ and planet–host projected separation $a_\perp$. See Jung et al. (2021) for a description of the Galactic model and Bayesian techniques. However, in most cases we still have to decide how to combine these separate estimates into a single "quotable result." Moreover, in

Table 8
Physical Properties

Event Models	Physical Properties				Relative Weights	
					Gal.Mod.	χ^2
KB210712	$M_{\rm host}$ ($M_\odot$)	$M_{\rm planet}$ ($M_\oplus$)	D_L (kpc)	$a_\perp$ (au)		
$u_0 > 0$	$0.23^{+0.12}_{-0.07}$	$39.90^{+20.60}_{-11.90}$	$3.20^{+0.91}_{-0.68}$	$2.29^{+0.64}_{-0.42}$	1.000	0.374
$u_0 < 0$	$0.14^{+0.06}_{-0.04}$	$25.76^{+11.28}_{-7.11}$	$2.08^{+0.65}_{-0.42}$	$1.57^{+0.42}_{-0.26}$	0.055	1.000
Adopted	$0.22^{+0.12}_{-0.07}$	$38.19^{+20.52}_{-12.24}$	$3.09^{+0.94}_{-0.75}$	$2.22^{+0.66}_{-0.48}$		
KB210909	$M_{\rm host}$ ($M_\odot$)	$M_{\rm planet}$ ($M_{\rm J}$)	D_L (kpc)	$a_\perp$ (au)		
	$0.38^{+0.30}_{-0.20}$	$1.26^{+1.01}_{-0.66}$	$6.48^{+1.00}_{-1.38}$	1.75 ± 0.42		
KB212478	$M_{\rm host}$ ($M_\odot$)	$M_{\rm planet}$ ($M_{\rm J}$)	D_L (kpc)	$a_\perp$ (au)		
$u_0 > 0$	$0.20^{+0.09}_{-0.05}$	$0.91^{+0.42}_{-0.24}$	2.86 ± 0.68	1.83 ± 0.30	0.866	0.992
$u_0 < 0$	$0.20^{+0.10}_{-0.05}$	$0.90^{+0.42}_{-0.24}$	3.06 ± 0.71	1.87 ± 0.31	1.000	1.000
Adopted	$0.20^{+0.10}_{-0.05}$	$0.90^{+0.42}_{-0.24}$	2.97 ± 0.72	1.85 ± 0.31		
KB211105	$M_{\rm host}$ ($M_\odot$)	$M_{\rm planet}$ ($M_{\rm J}$)	D_L (kpc)	$a_\perp$ (au)		
No I_L constraint						
Local 1	0.63 ± 0.33	1.30 ± 0.68	4.55 ± 1.67	$3.64^{+0.93}_{-1.19}$	1.000	1.000
Local 2	0.63 ± 0.33	1.28 ± 0.67	4.48 ± 1.66	$2.82^{+0.72}_{-0.93}$	0.975	0.129
$I_L > I_B$ constraint						
Local 1	0.61 ± 0.31	1.27 ± 0.65	4.62 ± 1.65	$3.60^{+0.89}_{-1.14}$	0.946	1.000
Local 2	0.61 ± 0.32	1.24 ± 0.64	4.55 ± 1.64	$2.78^{+0.69}_{-0.89}$	0.920	0.129
$\lvert I_L - I_B \rvert < 0.2$ const.						
Local 1	$1.17^{+0.42}_{-0.31}$	$2.43^{+0.88}_{-0.64}$	4.14 ± 1.38	4.79 ± 0.87	0.023	1.000
Local 2	$1.17^{+0.42}_{-0.31}$	$2.37^{+0.85}_{-0.63}$	4.15 ± 1.38	3.70 ± 0.67	0.024	0.129
Adopted	0.63 ± 0.33	1.30 ± 0.68	4.54 ± 1.67	3.54 ± 1.06		

several cases, we also discuss how the nature of the planetary systems can ultimately be resolved by future AO observations. Hence, we discuss each event separately below.

5.1. KMT-2021-BLG-0712

Because $\theta_{\rm E}$ and $\pi_{\rm E}$ are both measured, it might appear that we could directly estimate the lens mass, $M = \theta_{\rm E}/\kappa\pi_{\rm E}$, and distance, $D_L = {\rm au}(\pi_{\rm E}\theta_{\rm E} + \pi_S)$, where $\pi_S \sim 120$ mas. However, because the two parallax solutions in Table 2 differ significantly, this procedure yields two different pairs of values: $(M/M_\odot,\ D_L/{\rm kpc}) = (0.18,\ 2.7)$ and $(0.11,\ 1.7)$. Moreover, because the errors in $\pi_{\rm E}$ are not negligible, phase-space considerations will generally favor more distant lenses within each solution. Furthermore, they will also favor the $u_0 > 0$ solution owing to its smaller $\pi_{\rm E}$. Hence, in order to take account of phase space and properly weight these two solutions, it is essential to conduct a Bayesian analysis. As constraints, we include $t_{\rm E}$ (Table 2), $\boldsymbol{\pi}_{\rm E}$ (Equations (6) and (7)), and $\theta_{\rm E}$ (Equations (15) and (16)). Note that the parallax error ellipses can also be expressed in equatorial coordinates, in which case the errors in the cardinal directions are given by Table 2 and the correlation coefficients are $+0.53$ and -0.73 for the $u_0 > 0$ and $u_0 < 0$ solutions, respectively. Formally, we also include the constraint on the lens flux $I_L > I_B = 19.21$, although as a practical matter it plays no role because the $\pi_{\rm E}$ and $\theta_{\rm E}$ measurements already imply $I_L \gtrsim 23$.

The results shown in Table 8 confirm the naive reasoning given above. First, the median lens distances are larger than the naive estimates, while the 68% confidence intervals are skewed toward even larger distances. Second, because $\theta_{\rm E} \equiv \sqrt{\kappa M \pi_{\rm rel}}$ is better constrained than $\pi_{\rm E}$, the "phase-space pressure" toward larger D_L (smaller $\pi_{\rm rel}$) also pushes the host masses up relative to the naive estimates and likewise causes them to be asymmetric toward even higher values. Third, the "more populated" regions of phase space that are available to the $u_0 > 0$ solution, due to its smaller $\pi_{\rm E}$, give it substantially higher Galactic-model weight, which more than compensates for its slightly worse χ^2.

The mass and distance distributions for the two solutions are shown in the top two rows of Figure 11.

The planet is intermediate in mass between Neptune and Saturn and orbits a mid- to late M dwarf at about 3 kpc.

5.2. KMT-2021-BLG-0909

For this event, there is only one solution, for which there are two constraints: $t_{\rm E} = 16.06 \pm 0.73$ days (from Table 3) and $\theta_{\rm E} = 0.362 \pm 0.049$ mas (from Equation (17)). The mass and distance distributions are presented in the third row of Figure 11. These show that the system most likely lies in the Galactic bulge.

The planet is of Jovian mass and orbits a mid-M dwarf at about 6.5 kpc.

5.3. KMT-2021-BLG-2478

For this event, there are four constraints (on $t_{\rm E}$, $\pi_{\rm E}$, I_L, and ρ). The constraints on $t_{\rm E}$ and $\boldsymbol{\pi}_{\rm E}$ are given in Table 4, with the correlation coefficients for $\boldsymbol{\pi}_{\rm E}$ being -0.07 and -0.11 for $u_0 > 0$ and $u_0 < 0$, respectively. As discussed in Section 4.3, the constraint on lens light is $I_L > I_B = 18.15$.

As discussed in Sections 3.4 and 4.3, the constraints on ρ are given by the $\chi^2(\rho)$ envelope functions that are derived from the MCMC, which we implement as $\exp(-\chi^2(\rho)/2)$. See Figure 9.

Table 8 shows the results of the Bayesian analysis. The mass and distance are consistent at well under 1σ with the naive estimates given in Section 3.4.3 based on the relatively weak

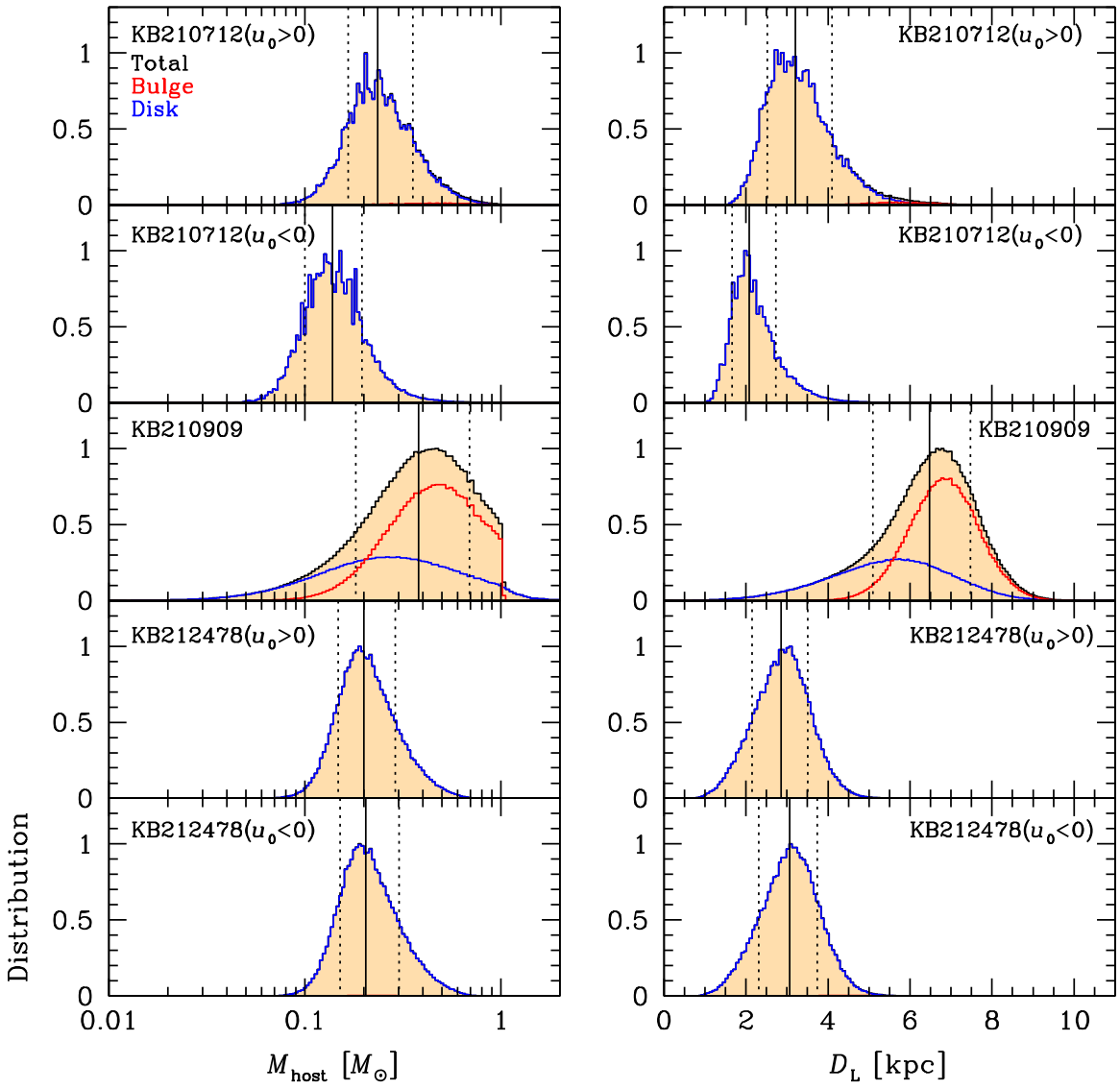

Figure 11. Host mass and system distance distributions from Bayesian analyses of various models (after imposing various constraints) for three of the events analyzed in this paper, KMT-2021-BLG-0712, KMT-2021-BLG-0909, and KMT-2021-BLG-2478. For the first and last of these events, there are two models that are consistent with the light-curve data. Bulge–lens and disk–lens distributions are shown in red and blue, respectively, while their total is shown in black.

minima shown in Figure 9. The reason is that ρ is strongly constrained toward higher values by the MCMC, while substantially lower values are strongly disfavored by the Bayesian priors because they would imply very nearby lenses.

The mass and distance distributions are shown in Figure 11. Bulge lenses are virtually excluded. The planet is of Jovian mass and orbits a late M dwarf at about 3 kpc.

5.4. KMT-2021-BLG-1105

For this event there are two well-established constraints (on $t_{\rm E}$ and $\theta_{\rm E}$), as well as one potential constraint (on I_L) that remains to be investigated. The first, from Table 5, is $t_{\rm E} = 35.0 \pm 1.9$ days (or $t_{\rm E} = 35.4 \pm 1.9$ days). The second, as discussed in Section 4.4, is implemented via a $\chi^2(\rho)$ envelope function (Figure 10), together with an estimate for each simulated event with Einstein radius $\theta_{{\rm E},i}$, of $\rho_i = \theta_{\rm ast}/\theta_{{\rm E},i}$, with $\theta_{\rm ast}$ given by Table 7.

The potential constraint on I_L comes from the limit $I_L \geqslant I_{B,{\rm cal}}$, where we calibrate the blend as $I_{B,{\rm cal}} = I_B - I_{\rm cl} + I_{{\rm cl},0} + A_I = 18.86$, with $I_B = 19.00$ and $I_{\rm cl} - I_{{\rm cl},0} = 2.88$ coming from Table 7 and $A_I = 2.75$ coming from the KMT web page. The reason that this constraint is "potential" is that our investigation in Section 4.4 showed that the lens could be the origin of this blended light, in which case using it as a limit to exclude simulated events would bias the result toward lower masses. Thus, to check whether the "blend = lens" scenario is plausible within a Bayesian context, we first carry out the Bayesian analysis both with and without this constraint.

The results are given in Table 8 and illustrated in Figure 12. They show that the Bayesian estimates hardly change between the two cases. However, they also show that roughly 5% of the Galactic weight is eliminated by the flux constraint. This indicates that the "blend = lens" hypothesis is consistent with the Bayesian priors at about the 2σ level (without yet taking into consideration the low probability of finding a random field star $\lesssim 0.''1$ of the event).

Therefore, we also conduct an additional Bayesian simulation under the constraint $|I_L - I_B| < 0.2$. Note that the width of this interval is somewhat arbitrary: we just seek to distinguish

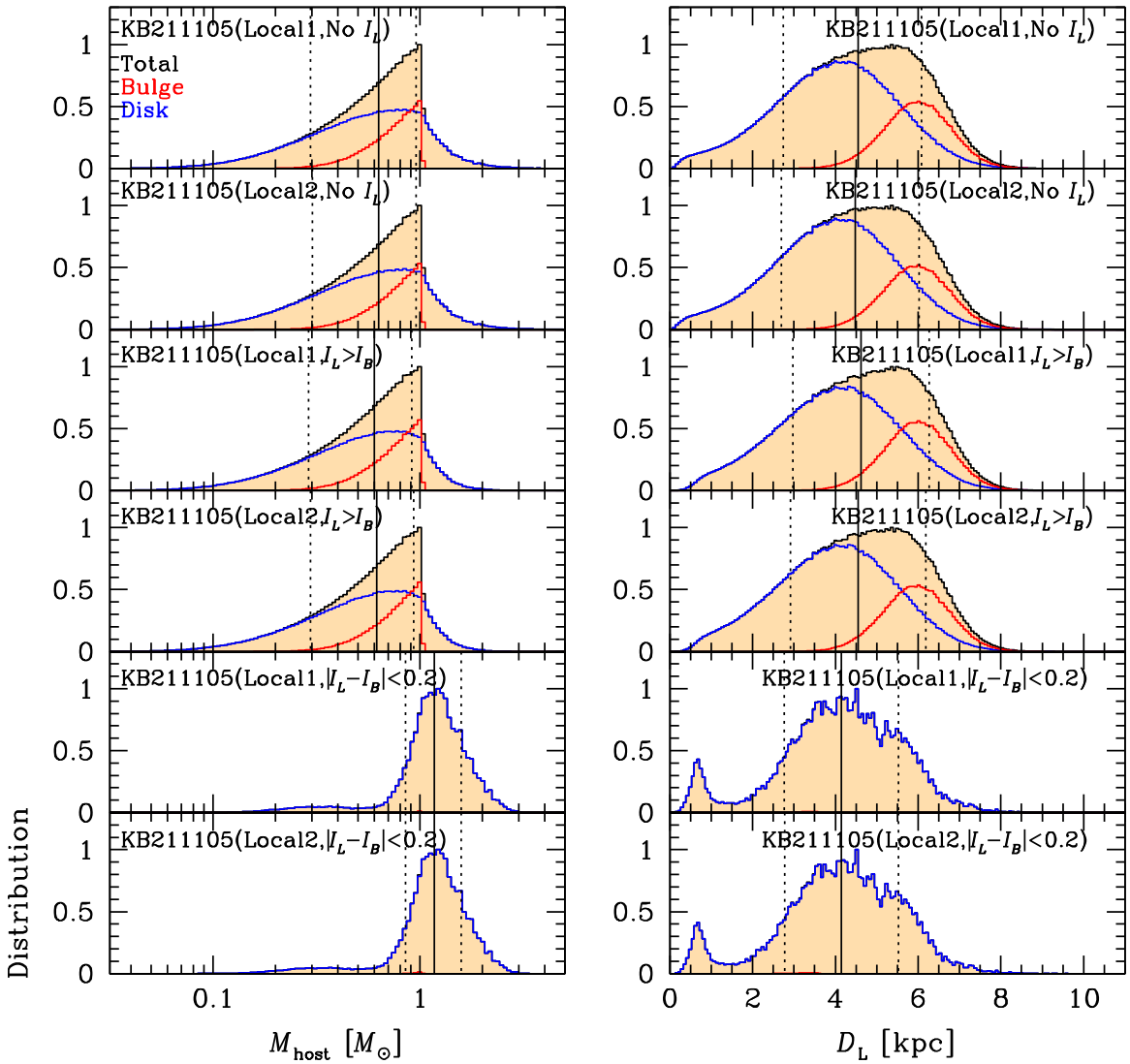

Figure 12. Host mass and system distance distributions from Bayesian analyses of two models (after imposing three different sets of constraints) for KMT-2021-BLG-1105. Color-coding is the same as in Figure 11.

simulated events that are roughly consistent with the "blend = lens" hypothesis from those that are not. The first point to note is that the host is a roughly solar-mass star at $D_L \sim 4$ kpc. That is, it is substantially more massive than the unconstrained estimate, but roughly at the same distance. Second, at this distance, the lens system is located about 200 pc above the Galactic plane, and it therefore lies behind almost all the dust. Because $[(V-I)_B - (V-I)_{\rm cl} = -0.46$ (see Figure 8), this implies $(V-I)_{B,0} \simeq 0.60$, which is a very plausible value for a solar-mass (or slightly more massive) star.

Thus, we find that the "blend = lens" scenario is consistent with all the available constraints. On the other hand, the hypothesis that the blend is a companion to the lens is also plausible. In this case, the $\sim 0\farcs1$ astrometric offset would be explained by the companion being roughly 400 au from the host (rather than corruption of the astrometry by a faint field star).

We conclude that the blend is very likely to be either the host or a companion to the host. These scenarios could easily be distinguished by high-resolution imaging by either AO on 8 m class telescopes or the HST. That is, a bright companion at $\sim 0\farcs1$ would easily be detected, which would verify the "blend = companion" scenario, while a contaminating random field star at several tenths of an arcsecond (verifying the "blend = lens" scenario) would be even more easily resolved. However, pending such a resolution, we advocate using the "no *I* constraint" Bayesian analysis, which we treat as "Adopted" in Table 8.

If future high-resolution imaging (which could be done immediately) confirms the "blend = lens" hypothesis, then KMT-2021-BLG-1105Lb would be one of the rare microlensing planets that could be further studied using the radial velocity (RV) technique. If we adopt $M \simeq 1.1\,M_\odot$, which is consistent with both Table 8 and $(V-I)_{B,0} = 0.60$, and we adopt $\pi_{\rm rel} \sim 0.13$ mas (consistent with Table 8), then $\theta_{\rm E} \equiv \sqrt{\kappa M \pi_{\rm rel}} \simeq 1.1$ mas and $a_\perp \sim 5.3$ au (or 4.1 au). Considering that the semimajor axis is likely to be larger than the projected separation by a factor $\sim 1.5^{1/2} = 1.22$, the orbital periods for Locals 1 and 2 are likely of order 16 and 11 yr, respectively, with RV amplitudes of order $v \sin i \sim (25\ {\rm m\ s^{-1}}) \sin i$ and $\sim (30\ {\rm m\ s^{-1}}) \sin i$. Adopting $A_I/E(V-I) \sim 1.3$ from Figure 6 of Nataf et al. (2013), we obtain $V_{B,{\rm cal}} = I_{B,{\rm cal}} + (V-I)_0 +$

$A_I/1.3 \simeq 21.6$. Hence, assuming that future high-resolution imaging confirms that the blend is the lens, it will be feasible to carry out RV measurements of the requisite precision on this (I, V) $\simeq$ (18.9, 21.6) star on 30 m class telescopes.

6. Discussion

This is the second in a series of papers that aims to publish all planets (and possible planets) that are detected by eye from 2021 KMTNet data and that are not published for other reasons. Together, we have presented a total of eight such planets. In the course of these efforts, we identified a total of seven other events that warranted detailed investigation but did not yield good planetary (or possibly planetary) solutions. Among the total of 15 events that were analyzed to prepare these two papers, none were possibly planetary but ultimately ambiguous. We have summarized that eight other by-eye KMTNet planets have been published, of which seven will likely enter the AnomalyFinder statistical sample, as well as one possible planet. Thus, to date, there are a total of 16 planets from 2021 that are seemingly suitable for statistical analysis. These work-in-progress figures can be compared to 2018, which is the only year with a complete sample of KMTNet planets, as cataloged by Gould et al. (2022a) and Jung et al. (2022). In that case, of the 33 planets found by AnomalyFinder that were suitable for statistical studies, 22 were discovered by eye, whereas of the 8 possible planets, 3 were discovered by eye. That is, there were 22/3 discoveries for the full 2018 yr compared to 16/1 discoveries for the partial 2021 yr. Hence, this ongoing work is broadly consistent with the only previous comprehensive sample.

This research has made use of the KMTNet system operated by the Korea Astronomy and Space Science Institute (KASI), and the data were obtained at three host sites of CTIO in Chile, SAAO in South Africa, and SSO in Australia. This research was supported by the Korea Astronomy and Space Science Institute under the R&D program (project No. 2022-1-830-04) supervised by the Ministry of Science and ICT. Work by C.H. was supported by grant 2017R1A4A101517 of the National Research Foundation of Korea. Work by H.Y. and W.Z. was partly supported by the National Science Foundation of China (grant No. 12133005). J.C.Y. acknowledges support from U.S. NSF grant No. AST-2108414. Y.S. acknowledges support from BSF grant No. 2020740.

ORCID iDs

Yoon-Hyun Ryu https://orcid.org/0000-0001-9823-2907
Hongjing Yang https://orcid.org/0000-0003-0626-8465
Michael D. Albrow https://orcid.org/0000-0003-3316-4012
Sun-Ju Chung https://orcid.org/0000-0001-6285-4528
Cheongho Han https://orcid.org/0000-0002-2641-9964
Kyu-Ha Hwang https://orcid.org/0000-0002-9241-4117
Youn Kil Jung https://orcid.org/0000-0002-0314-6000
Yossi Shvartzvald https://orcid.org/0000-0003-1525-5041
Jennifer C. Yee https://orcid.org/0000-0001-9481-7123
Weicheng Zang https://orcid.org/0000-0001-6000-3463
Seung-Lee Kim https://orcid.org/0000-0003-0562-5643
Chung-Uk Lee https://orcid.org/0000-0003-0043-3925
Byeong-Gon Park https://orcid.org/0000-0002-6982-7722
Richard W. Pogge https://orcid.org/0000-0003-1435-3053

References

Alard, C., & Lupton, R. H. 1998, ApJ, 503, 325
Albrow, M. D. 2017, Michaeldalbrow/Pydia: InitialRelease On Github v1.0.0, Zenodo, doi:10.5281/zenodo.268049
Albrow, M. D., Horne, K., Bramich, D. M., et al. 2009, MNRAS, 397, 2099
An, J. H., Albrow, M. D., Beaulieu, J.-P., et al. 2002, ApJ, 572, 521
An, J. H., & Gould, A. 2001, ApJL, 563, L111
Benedict, G. F., Henry, T. J., Franz, O. G., et al. 2016, AJ, 152, 141
Bensby, T., Yee, J. C., Feltzing, S., et al. 2013, A&A, 549, A147
Bessell, M. S., & Brett, J. M. 1988, PASP, 100, 1134
Dong, S., Gould, A., Udalski, A., et al. 2009, ApJ, 695, 970
Gaudi, B. S. 1998, ApJ, 506, 533
Gould, A. 1992, ApJ, 392, 442
Gould, A. 2000, ApJ, 542, 785
Gould, A. 2004, ApJL, 606, 319
Gould, A. 2022, arXiv:2209.12051
Gould, A., Han, C., Zang, W., et al. 2022a, A&A, 664A, 13
Gould, A., Jung, Y. K., Hwang, K.-H., et al. 2022b, JKAS, 55, 173
Gould, A., Zang, W., Mao, S., & Dong, S. 2021, RAA, 21, 133
Griest, K., & Hu, W. 1992, ApJ, 397, 362
Han, C. 2006, ApJ, 638, 1080
Han, C., Bond, I. A., Yee, J. C., et al. 2022a, A&A, 658A, 94
Han, C., Doeon, K., Gould, A., et al. 2022b, A&A, 664A, 33
Han, C., Doeon, K., Yang, H., et al. 2022c, A&A, 664A, 114
Han, C., & Gould, A. 1997, ApJ, 480, 196
Han, C., Gould, A., Bond, I. A., et al. 2022d, A&A, 662A, 70
Han, C., Gould, A., Doeon, K., et al. 2022e, A&A, 663A, 145
Han, C., Gould, A., Hirao, Y., et al. 2021a, A&A, 655A, 24
Han, C., Udalski, A., Kim, D., et al. 2021b, A&A, 650A, 89
Herrera-Martin, A., Albrow, A., Udalski, A., et al. 2020, AJ, 159, 134
Holtzman, J. A., Watson, A. M., Baum, W. A., et al. 1998, AJ, 115, 1946
Hwang, K.-H., Udalski, A., Bond, I. A., et al. 2018, AJ, 155, 259
Hwang, K.-H., Zang, W., Gould, A., et al. 2022, AJ, 163, 43
Jung, Y. K., Han, C., Udalski, A., et al. 2021, AJ, 161, 293
Jung, Y. K., Zang, W., Han, C., et al. 2022, AJ, 164, 262
Kervella, P., Thévenin, F., Di Folco, E., & Ségransan, D. 2004, A&A, 426, 297
Kim, D.-J., Hwang, K.-H., Shvartzvald, Y., et al. 2018b, arXiv:1806.07545
Kim, S.-L., Lee, C.-U., Park, B.-G., et al. 2016, JKAS, 49, 37
Minniti, D., Lucas, P. & VVV Team 2017, yCAT, 2348, 0
Nataf, D. M., Gould, A., Fouqué, P., et al. 2013, ApJ, 769, 88
Paczyński, B. 1986, ApJ, 304, 1
Park, B.-G., DePoy, D. L., Gaudi, B. S., et al. 2004, ApJ, 609, 166
Parsons, S. G., Gänsocle, B. T., Marsh, T. R., et al. 2018, MNRAS, 481, 1083
Poindexter, S., Afonso, C., Bennett, D. P., et al. 2005, ApJ, 633, 914
Ryu, Y.-H., Jung, Y. K., Yang, H., et al. 2022, AJ, 164, 180
Schechter, P. L., Mateo, M., & Saha, A. 1993, PASP, 105, 1342
Smith, M. C., Mao, S., & Paczyński, B. 2003, MNRAS, 339, 925
Szymański, M. K., Udalski, A., Soszyński, I., et al. 2011, AcAau, 61, 83
Tomaney, A. B., & Crotts, A. P. S. 1996, AJ, 112, 2872
Wang, H., Zang, W., Zhu, W., et al. 2022, MNRAS, 510, 1778
Yang, H., Zang, W., Gould, A., et al. 2022, MNRAS, 516, 1894
Yoo, J., DePoy, D. L., Gal-Yam, A., et al. 2004, ApJ, 603, 139
Zang, W., Hwang, K.-H., Udalski, A., et al. 2021b, AJ, 162, 163
Zang, W., Yang, H., Han, c., et al. 2022, MNRAS, 515, 928
Zhang, K., & Gaudi, B. S. 2022, ApJL, 936, L22